Ge Gao · Mohamed A. Meguid · Luc E. Chouinard · Weiwei Zhan

Dynamic disintegration processes accompanying transport of an earthquake-induced landslide

Abstract Aiming to understand the dynamic disintegration and transport behavior of an earthquake-induced landslide, a dynamic discrete element method has been employed to analyze the Wangjiayan landslide triggered by the 2008 Ms 8.0 Wenchuan earthquake. Absorbing boundary condition is used for the seismic wave transmission and reflection at the slope base. The numerical results show that under seismic loading, internal rock damage initiates, propagates, and coalesces progressively along the weak solid structure and subsequently leads to fragmentation and pulverization of the slope mass. This can be quantitatively interpreted with the continuously rapid increase of the damage ratio and sudden decline of growth ratio of the number of fragments after the peak seismic shaking. During emplacement evolution, fragmented deformation patterns within the translating joint-defined granular assemblies are affected by the locally high dilatancy with a simultaneous occurrence of highly energetic collisions related to the action of shearing, and this can be quantified by the enhancement of particle kinematic activities (high vibrational and rotational granular temperatures) and intense fluctuations of location-dependent global dispersive stress. In this process, slope destabilized and transports downward in a rapid pulsing motion as friction bonds are locally and continually overcome by the seismic- and gravity-induced shear forces. The joint-determined fragment network before movement initiation and the final fragmented depositions after the rapidly sheared transport have been systematically investigated by fragment statistics (fragment size distribution, fragment mass distribution, and fractal dimension) and morphometric characters (fragment shape isotropy) to offer new insights into the disintegration characteristics of the earthquake-induced catastrophic mass movements.

Keywords Earthquake-induced landslide · Discrete element method · Absorbing boundary condition · Dilatancy · Fragmentation

Introduction

Earthquake-induced landslides are among the natural hazards that can pose serious threats to communities and infrastructures. Many catastrophic landslides of this type have recently occurred worldwide, in particular, the 2008 Mw 7.9 Wenchuan earthquake has triggered more than 56,000 landslides in steep mountainous terrain covering an area of about 41,750 km² (Wang et al. 2009; Dai et al. 2011). The landslides directly caused more than 20,000 fatalities (Yin et al. 2009). In light of the catastrophic instability and disastrous consequence, there has been an increasing interest in the study of earthquake-triggered landslides; however, much uncertainty still exists about co-seismic slope fragmentation and emplacement mechanism.

The landslide is always associated with rock fragmentation together with high spreading velocities, long runouts, and energy release; however, the process of fragmentation is rarely directly observed as it occurs in nature due to the destructive capacity and unpredictability of the landslide (Wang et al. 2018; Davies et al. 2020). To understand the complex interplay between the disintegration process and the transport mechanism, the related research has been extensively performed by means of field investigations in real landslide deposits, experimental studies of a fragmentable, brittle, solid rock analogue material sliding over a simple slope geometry, and numerical simulations.

Based on field investigations of deposits of landslides, Crosta et al. (2007) measured the representative rock block size distribution at the source and deposit area of the 1987 Val Pola rock avalanche and quantified their relationships with the fragmentation process and the corresponding energy consumption, indicating that more than a single comminution process acted during rock avalanche emplacement. Through a detailed mechanical analysis of the microscopic surface texture on quartz grains sampled from the basal facies of two earthquake-triggered landslides, Wang et al. (2015) proposed that both the overburden pressure and the self-excited vibration play dominant roles in the occurrence of particle dynamic fragmentation in the basal facies. Perinotto et al. (2015) combined field studies, grain size, exoscopic, and new morphometric measurements using fractal dimension and circularity indicators bringing new insights to the role of dynamic disintegration processes on the extreme mobility of landslides.

Experimental studies using a series of analogue models under different testing conditions show that fragmentation can increase the travel length of the front of landslide deposits (Bowman et al. 2012; Haug et al. 2016) and produce fine materials that may act as a lubrication (De Blasio and Elverhøi 2008; Wang et al. 2017; Zhao and Crosta 2018) or dispersive stresses from exploding fragments may effectively reduce the normal stress at the base (Davies and McSaveney 2009). This process involves energy losses (Haug et al. 2016) and an increase in volumetric fraction of fine-grained material (Langlois et al. 2015) affecting both the fragment trajectory and dynamic runouts (De Blasio and Crosta 2014; 2015).

Field investigations and physical models are, therefore, to infer dynamic disintegration and transport characteristics a posteriori from the deposits (Pollet and Schneider 2004; Sassa et al. 2004; Dunning 2006; Locat et al. 2006; Ruiz-Carulla et al. 2015, 2017; Zhang and McSaveney 2017; Dufresne and Geertsema 2020). However, due to the lack of recordings on the transport processes and opportunities to observe the interiors of landslides (Zhang et al. 2019), moreover, these methods suffer from a large number of assumptions and simplifications (Dammeier et al. 2011), and the propagation mechanisms and dynamic fragmentations of such events are still not completely understood and a lively discussion continues on.

Therefore, numerical simulation provides an alternative avenue to simulate the landslide transport and deposition. The most commonly used numerical simulations are based on continuum or discontinuum method. Continuum methods, such as the

smoothed particle hydrodynamics (SPH) model, the depth-averaged numerical (DAN) model, and the finite element model (FEM), are able to simulate the dynamic movements of actual landslides (Eberhardt et al. 2004; Hungr and McDougall 2009; Yin et al. 2015; Yerro et al. 2016). However, continuum-based numerical models often fail to reproduce the progressive failure of rock slopes, especially the dynamics of kinematic release accompanying complex internal distortion, dilation, and fracture (Stead et al. 2006).

Unlike the continuum-based models, the discontinuum-based approaches, such as the discrete element method (DEM) and discontinuous deformation analysis (DDA), do not limit the scale of separation and displacement behavior of individual elements and can simulate the entire landsliding process from initiation, propagation to deposition. However, the complexity of the contact detection in the DDA program leads to the computational inefficiency (Wu et al. 2009a; Wu and Chen 2011), besides, neglection of the gravity and too large assigned density for the bedrock provide an unrealistic scenario for landslide simulation.

The discrete element method (DEM) has been broadly categorized into particulate and blocky systems. In the discrete element analysis of blocky systems, deformable blocks are represented by polygon and polyhedral. Although the use of a Voronoi tessellation partitioning approach can allow the building of discrete models with explicit representation of discontinuities, the limitations arise when dealing with incomplete block formation (Elmo et al. 2013). In contrast, the discrete element analysis of a particulate system has been demonstrated to be an effective tool that can study the micromechanisms underlying the fracturing behavior of rock material. In addition, it is suitable as an engineering tool to analyze the large deformation of rock slope and the subsequent landslides (Wang et al. 2003; Thompson et al. 2009; Cagnoli and Piersanti 2015; Borykov et al. 2019). Langlois et al. (2015) employed a two-dimensional DEM simulation to study the failure, collapse, and flow of brittle granular column over a horizontal surface for understanding dynamic rock fragmentation in a landslide. They suggest that the runout distance is higher when the deposit is highly fragmented, which confirms previous hypotheses proposed by Davies et al. (1999). Zhao et al. (2018) performed three-dimensional DEM analysis of a multiple arrangement of jointed rock blocks sliding over a simple slope geometry for demonstrating the role of rock discontinuity at ruling fracture nucleation and fragmentation during landslide dynamic evolution. They report that runout distance decreases with the increase of initial fragmentation intensity.

Notwithstanding these advancements, less attention has been paid to studying the dynamic disintegration process and transport mechanism of earthquake-induced landslides with complex geological and geomorphological settings (Meunier et al. 2007; Zhao and Crosta 2018; Wei et al. 2019). In recent years, some of the reported studies related to modeling earthquake-induced landslides (e.g., Tang et al. 2009; Lo et al. 2011; Yuan et al. 2014, 2015; Zhou et al. 2015; Scaringi et al. 2018) focused on the kinematic behavior and deformation mechanics of the system only throughout simple recording of the displacements and velocities; however, little details were provided unraveling the response of jointed rock materials during landslide emplacement subjected to intense seismic shaking from insights into transport mechanism and dynamic disintegration.

A case study of a landslide that took place in China in 2008 is investigated and used for the validation of the developed DE numerical model. A description of the geological setting in the area of the rock material is first presented. A series of numerical simulations is then performed to examine the effect of using absorbing boundary conditions on the response of the model. The deformation evolution, disintegration process, and fragmentated deposition of the landslide under earthquake loading are then investigated focusing on the fracturing propagation, particle agitation, dispersed state, fractal behavior, and shape characteristics of the fragment populations.

Wangjiayan landslide

Wangjiayan landslide (104° 26′ 56.4″ E, 31° 49′ 33.6″ N), as one of the most catastrophic landslides induced by the 2018 Mw 7.9 Wenchuan earthquake, occurred in the south of old Beichuan County town Sichuan Province and resulted in approximately 1600 fatalities and ruined in dozens of buildings.

Geological and geomorphologic and setting

The Wangjiayan landslide area is on the hanging wall of the steeply dipping (60°–70°) Yingxiu-Beichuan rupture belt that extends through the toe of slope. It is approximately 130 km to the northeast of Wenchuan earthquake epicenter and approximately 400 m from Yinxiu-Beichuan fault (Yin et al. 2015; Li et al. 2016), as shown in Fig. 1a. Moreover, the complex structure of the slope is characterized by three main families of joints (J_1, J_2, and J_3), as shown in Fig. 1b. Two sets (J_1 and J_2) are sub-vertical, cut the slope transversely, and are responsible of the presence of prominent spurs; one set (J_3) has inclination almost parallel to the slope and define its main geometrical features.

From a lithological point of view, the exposed rocks in the Wangjiayan landslide area mainly include the Qingping Group ($\in_{1c}$) thin layers of sandstone, grey sandy shale, siltstone, and sandy slate of the Upper Cambrian. Its surface was covered by a quaternary eluvium-deluvial unconsolidated formation of thickness < 3 m.

The old Beichuan County, which belongs to the southeastern margin of erosional tectonic middle mountains and hill landforms within a valley characterized by steep slopes ranging from 30° to 50°, most of which are over 40° with sparse vegetation, as presented in Fig. 1c. Wangjiayan rock slope is located in the west part of the old Beichuan County in the region between the Mishi and Shenjia Valleys, as shown in Fig. 1c.

Failure mechanism and dynamic process

On the basis of the field investigation and the interpretation of topographic map and remote sensing images, downslope route, longitudinal profile, and characteristics of the Wangjiayan landslide are presented in Fig. 2. The landslide can be divided into the following two areas: the source area and deposition area (Fig. 2), and the corresponding possible failure process is as follows:

(1) The intense seismic shakings loosened and weakened the slope materials and further degraded the highly weathered rock mass. Consequently, the rock slopes shattered and collapsed at a high speed downwards directly towards the valley along the direction of 76°. This fast movement process did not
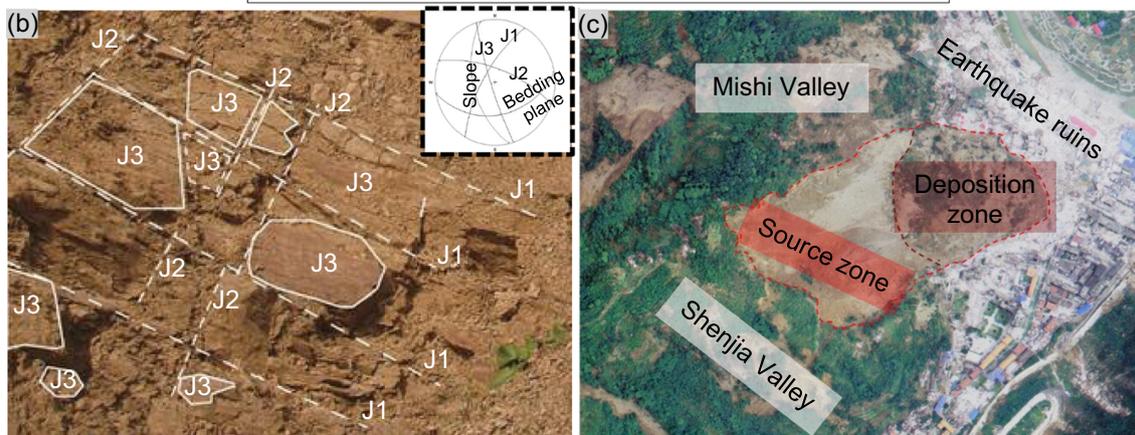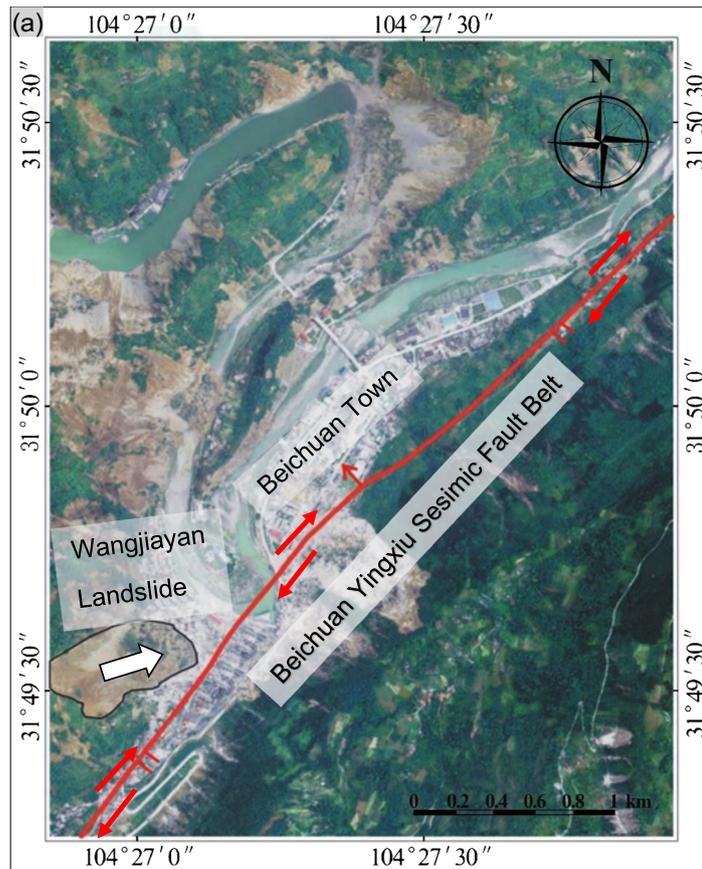
Fig. 1 **a** Geological and structural settings of the Wangjianyan landslide area: the fault belt location. **b** Details of the geological structural features. **c** Airborne remote sensing image of Wangjiayan landslide

only provide sufficient energy for the disintegration and fragmentation of the sliding mass but produced powerful air blast that destroyed the earthquake-damaged buildings to ruins at the outer margin of the deposition area (Fig. 2b). This is also evidenced by the existence of impact marks found in the deposited boulders (Fig. 2c).

(2) After colliding onto the valley, due to the low-gradient terrains, the displaced mass gradually lost momentum and exhibited radial spreading and flattening and finally

accumulated in a fan shape in the deposition area (Fig. 2d). The displaced materials ran out a horizontal distance of about 350 m with a descent of 320 m. Per site investigation, the deposited mass is composed mostly of grey, and grayish yellow rubble blocks containing gravel, boulders, and sandy soil, of which the parent rock was loose-dense thin layer of sandy shale, siltstone, and sandstone. About 60–90% of the rock debris was rubbles and gravels of highly weathered rocks

ranging from 10 to 20 cm in sizes and several large boulders (up to ~ 1 m in diameter).

The complete geometric and geologic information of the source area is summarized in Table 1.

The discrete element model

Based on the above observations from the field investigation, it is evidenced that the rock slide disintegrated rapidly during the downward motion along Wangjiayan mountain slope. According to Hungr et al. (2014), this landslide can be categorized as high-speed flow-like landslides, which is very suitable to be analyzed using the DEM. Model details and set-up procedure are discussed below.

DEM bonded particle model

In this distinct element analysis, the rock mass is simulated as an assembly of particles cemented together using the parallel bond

(a) Shenjia Valley / Mishi Valley / Detaching downward / Depositing / Air blasting / 405 m / 1150 m / 1000 m / N

(b)

(c)

(d)

Fig. 2 a An illustration of the downslope route of the Wangjiayan landslide. **b** The earthquake damaged buildings ruined into pieces by the turbulence generated by the rapid-moving rock mass. **c** The impact marks commonly existed in the deposited rock blocks. **d** Longitudinal profile of the Wangjiayan landslide

model (Itasca 2014). The parallel bond models have been widely used to study cracking and fragmentation of rock material. This type of particle bond acts as a conceptual cementitious material characterized by tensile and shear strength and normal and tangential stiffness (Potyondy and Cundall 2004). When the contact force exceeds either tensile or shear strength, the parallel bond breaks and a micro-crack forms between the particles. More specifically, if the tensile strength limit is exceeded, the bond breaks in tension. On the other hand, if the bond is not broken in tension, then the shear strength limit is enforced. More details related to the contact model can be found in Itasca (2014).

Finding the microparameters (radii, stiffness, and strength) of the particles and the parallel-bonded contacts to properly represent the rock material requires model calibration using standard tests to establish reliable relationships between the micro and macro responses. Based on the suggested calibration procedure (Potyondy and Cundall 2004), the micro-properties required for the DEM model are determined (Table 2) to achieve a realistic macro mechanical response of the rock mass. This is also consistent with the reported physical properties of the rock mass at the Wangjiayan landslide area (Cui et al. 2011). These properties are given in Table 3.

In addition, to study the dynamic behavior of the landslide, viscous damping needs to be taken into account to provide a reliable scenario (Gao and Meguid 2018). When viscous damping is active, normal and shear dashpots are added at each contact and act in parallel with the parallel bond model. Damping force is then calculated by the relative velocity at each contact and acts to oppose motion. The normal and shear viscous damping ratios are selected to be 0.21 and 0.02, respectively, as suggested by Feng et al. (2017).

Boundary conditions

Compared to previous studies (e.g., Tang et al. 2009; Yuan et al. 2014 and 2015; Zhao and Crosta 2018), the novelty in this landslide numerical analysis is the application of absorbing boundaries for avoiding the adverse effects of seismic wave reflection back into the model. The absorbing boundaries are created by adding dashpots in both the normal and shear directions along the base. Similar approach was successfully used by Zhang et al. (2014) and Gischig et al. (2015). This process is expressed in Eqs. (1) through (6) below:
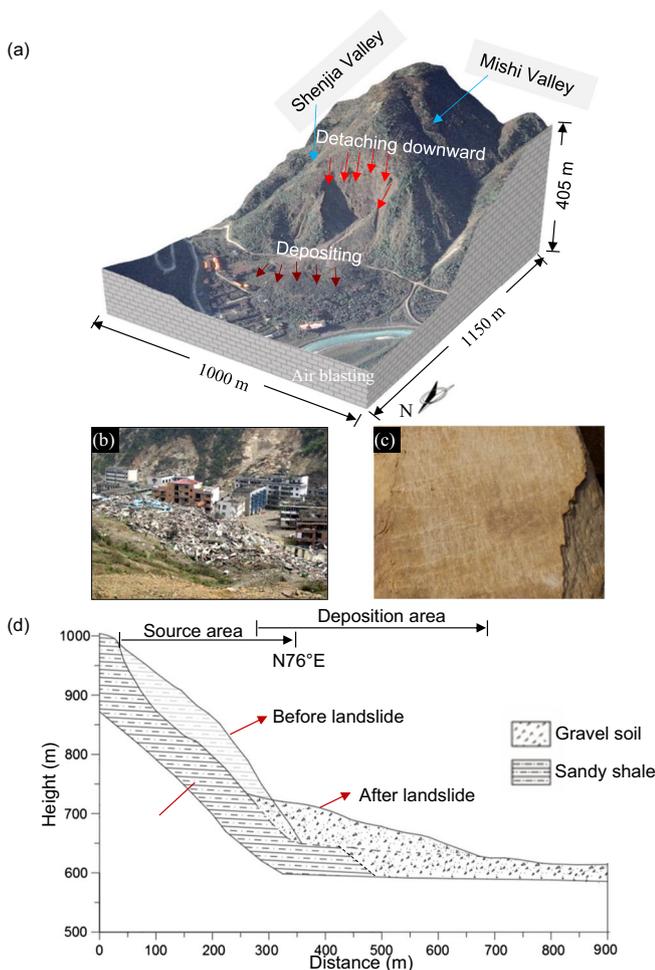
$$\sigma_n = -\rho V_p v_n \tag{1}$$

$$\sigma_s = -\rho V_s v_s \tag{2}$$

where σ_n and σ_s are the time-dependent normal and shear stresses at the base boundary, V_p and V_s are the P and S wave velocities, respectively, and v_n and v_s are the instantaneous normal and shear velocities of the boundary particles.

Replacing stresses, σ, using forces, F, such that $F = \sigma \times 2R$ in two dimensions. Equations (3) and (4) can be expressed in terms of boundary forces, F_n and F_s, and velocities, v_n and v_s:

$$F_n = -2R\rho V_p v_n \tag{3}$$

Table 1 Field information of source area and deposition area

Geometric and geologic conditions	
The source area	
The longitudinal extent	250–400
The lateral width	290–370 m and an average width 330 m
The head scarp in elevation	660 m
The toe of rupture surface in elevation	980 m
Height difference	320 m
The deposition area	
The longitudinal length	273 m
The lateral width	343 m
The area	52,422 m^2
The volume	1.4 Mm^3

$$F_s = -2R\rho V_s v_s \tag{4}$$

where R is the particle radius and ρ is the material density.

The following two equations are used to specify a given earthquake velocity in the vertical and horizontal directions.

$$F_n = 2R\rho V_p \left(2v_n^{equ} - v_n\right) \tag{5}$$

$$F_s = 2R\rho V_s \left(2v_s^{equ} - v_s\right) \tag{6}$$

where v_n^{equ} and v_s^{equ} are the applied velocity decomposed in the vertical and horizontal directions. It is worth noting that the factor of two for injected velocity (v_n^{equ}, v_s^{equ}) accounts for the equal partition of energy at the boundary.

According to the wave propagation theory, V_p and V_s can be determined using the following equations:

$$V_p = \sqrt{\frac{E(1-\nu)}{\rho(1+\nu)(1-2\nu)}} = \sqrt{\frac{3K + 4G}{3\rho}} \tag{7}$$

$$V_s = \sqrt{\frac{E}{2\rho(1+\nu)}} = \sqrt{\frac{G}{\rho}} \tag{8}$$

where E, K, G, ν, and ρ are the Young's modulus, Bulk modulus, shear modulus, Poisson's ratio, and density.

The effect of boundary conditions on the response to wave propagation is examined by analyzing a rock column that consists of a string of bonded particles with numerical parameters shown in Table 2. Three different boundary conditions are assigned to the top of the column, namely, absorbing (viscous or quiet) boundary, free boundary, and fixed boundary as illustrated in Fig. 3. The rock column is 60 m in length and 1 m in diameter and each particle has a radius of 0.5 m. Kuhlemeyer and Lysmer (1973) recommended at least eight to ten elements per wavelength of input motion for reliable dynamic computation. In this study, particles measuring 1/15 of the shortest wavelength are chosen as suggested by Gu and Zhao (2009) and Zhang et al. (2014). Ricker wavelets expressed in Eq. (9) with amplitude of 0.1 m/s and a time period of 3.0 s is injected from the bottom of the model and the response to different boundary conditions is calculated.

$$v_R(t) = A\left(1 - 2\pi^2 f^2 (t-1)^2\right) e^{-\pi^2 f^2 (t-1)^2} \tag{9}$$

where A is the amplitude and f is the central frequency of the signal.

To compare the column response to the investigated boundary conditions, five measurement points along the column, namely, A, B, C, D, and E, are used and the results are summarized in Fig. 4. The calculated velocity time history for the case of absorbing boundary is shown in Fig. 4a. The velocity at point E, located at

Table 2 Numerical parameters used in the discrete element analysis

Item	Micromechanical properties Rock mass
Ball-ball contact effective modulus	10.0 GPa
Ball stiffness ratio (k_n/k_s)	2.0
Ball friction angle	30°
Parallel bond effective modulus	10.0 GPa
Parallel bond stiffness ratio (k_n/k_s)	2.0
Parallel bond tensile strength	11.0 MPa
Parallel bond shear strength	22.0 MPa

**Table 3** Physical and mechanical properties of the rock mass

			Rock mass of Wangjiayan landslide		
Density (kg/m³)	Young's modulus (GPa)	Internal friction angle (°)	Compressive strength (MPa)	Brazilian tensile strength (MPa)	Poisson's ratio
2600	10.5	35	15.5	3.2	0.25

the top of the model, is found to be twice that of the input values of the Ricker wavelet which is consistent with the expected theoretical response at the boundary in this case. The absence of further oscillation at about 2.0 s indicates that the absorbing boundary has efficiently absorbed the induced energy. The slight oscillation seen after 2.0 s is related to the discrete nature of the medium (Itasca 2014). For the case of free boundary at point E, the velocity time history (Fig. 4b) reveals significant oscillation after 2.0 s which indicates the presence of wave reflection in this case. When fixed boundary was introduced (Fig. 4c), the velocity at

point E became zero with significant oscillation elsewhere after elapsed time of 2.0 s. It confirms that using fixed boundary results in wave reflection back into the model as no energy is absorbed at the boundary.

Model setup

Due to the parallel-processing optimization, PFC²ᴰ has been selected to build the discrete element model based on the profile map depicted in Fig. 2d. The steps taken to create the model are summarized as follows:
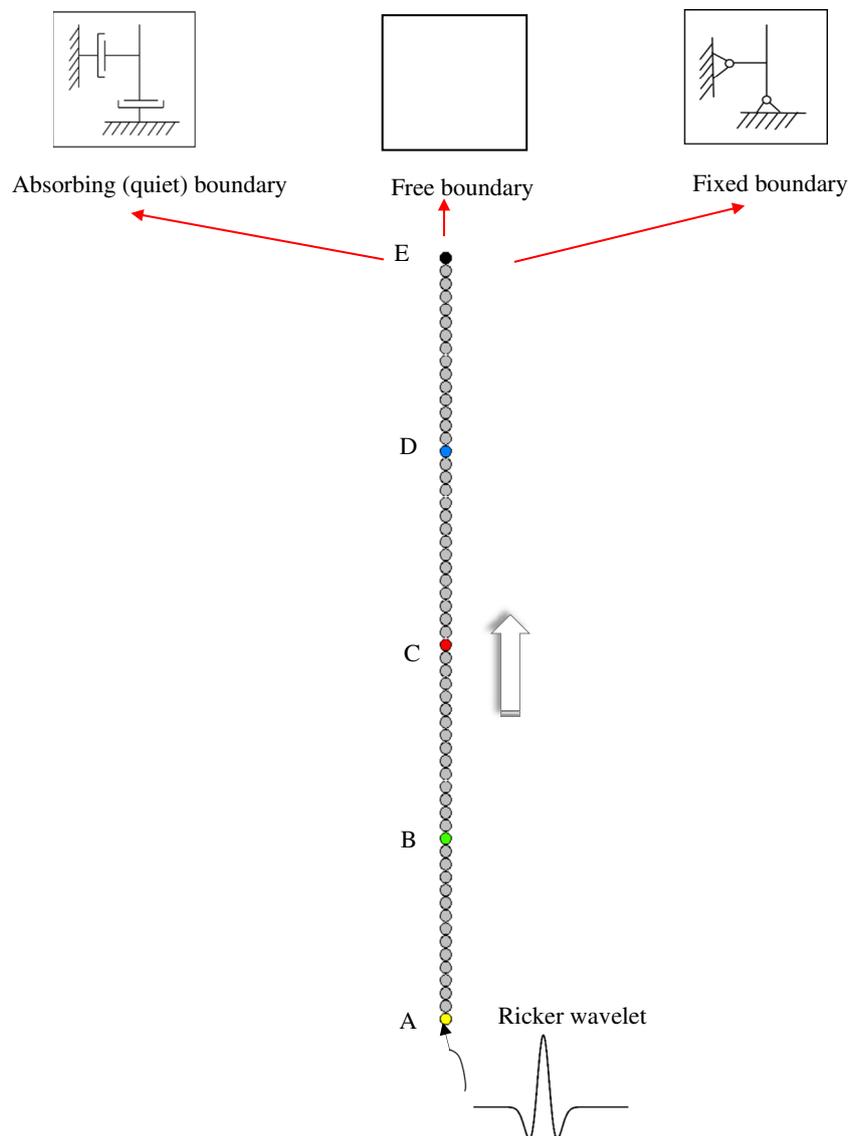
Fig. 3 Calculation model for a rock column using Ricker wavelet to demonstrate the different boundaries reacting
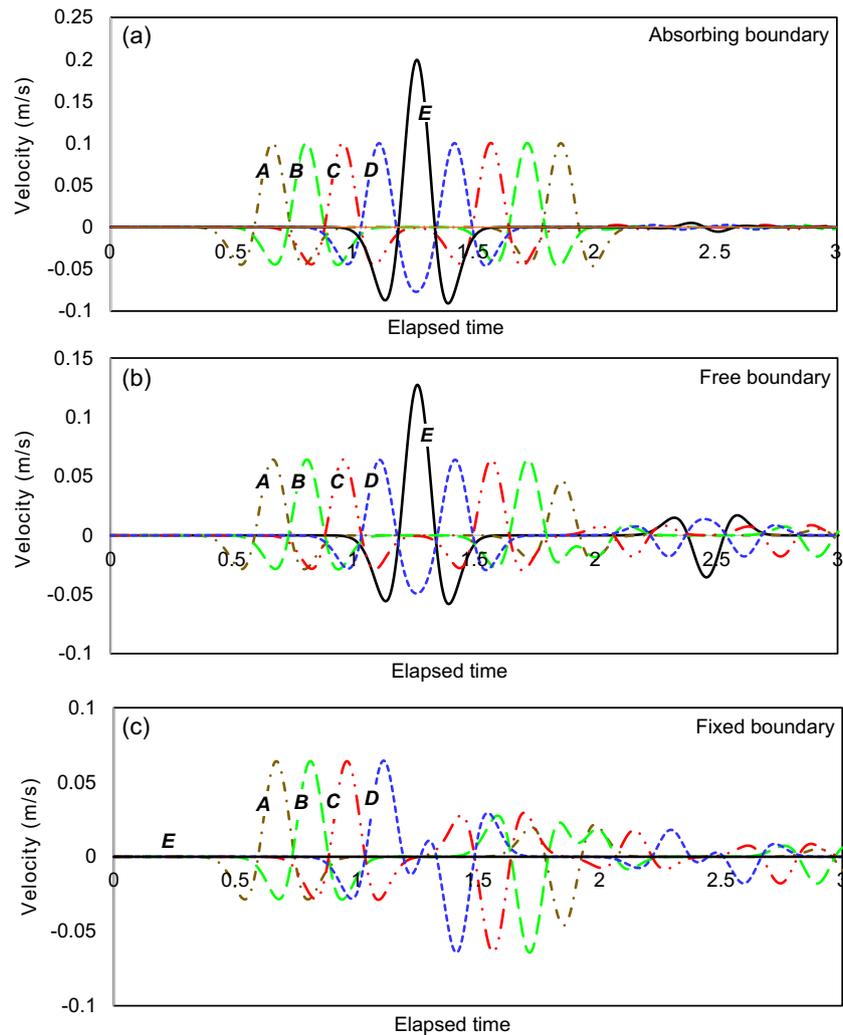
Fig. 4 Ricker wavelet time history calculated at five points along the rock column using DEM. **a** absorbing boundary; **b** free boundary; **c** fixed boundary

Generation The first step consists in generating an assembly of particles within the slope area to represent the rock material. As the modeled area in this case is relatively large, efforts are made to keep the computational cost at a reasonable level by using ranges of particle sizes that are relatively small near the zone of the sliding mass and larger particles elsewhere in the model. Thus, the sizes of the discrete elements (disk) are chosen such that the minimum diameter is 1.0 m in the source area and increases to 2.5 m within the rest of the model (the bedrock) as shown in Fig. 5a. In addition, the size ratio r_{max}/r_{min} of the rigid particles numbers 1.6 to prevent a reorganization of the particles within a closed-packed lattice (Imre et al. 2010). A total of 30286 elements are used in the model including 11069 and 19217 elements for the source area and the bedrock, respectively.

Bond installation Linear contact model is first assigned to all distinct elements and the model is cycled to equilibrium to ensure that a steady-state condition is achieved. After the system reaches equilibrium, the generated assemblies of particles in both the bedrock and the source area are assigned linear parallel-bonded

contacts to simulate the rock material. The microparameters for particles in the simulation are adopted from the aforementioned calibration. It is worth noting that the interparticle bonds in the bedrock need to be large enough to effectively represent the rock bridges between adjacent particles, contributing enough cohesion to the intact sandy slate and shale. To better visualize the emplacement process of the landslide, four layers are painted using different colors, as shown in Fig. 5a.

Discontinuity During the third step, joint sets are implanted into the numerical model. On account of complexity of actual rock mass structure, it is difficult to accurately reflect and model field conditions. In fact, the persistence, pattern, and orientation of joint sets in real natural rock slopes vary spatially and small discontinuities are also contributing to the degradation of rock mass strength. However, modeling the representative joint sets is in essence for understanding the performance of the DE analysis on the failure, runout, and fragmentation behavior of landslides. Therefore, in this study, three main joint sets are introduced in the 2D simulation model, including the joint sets J_1 (dip 68°, dip
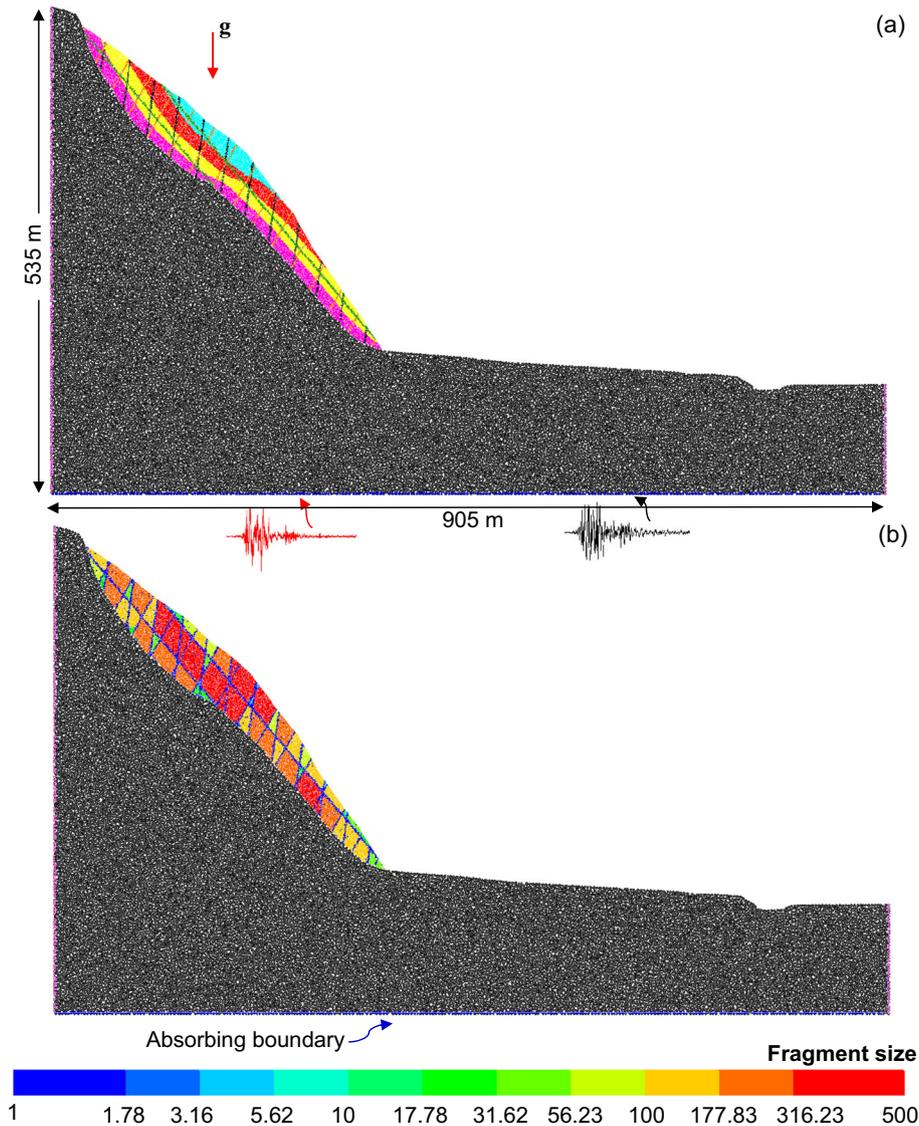
Fig. 5 a Two-dimensional discrete element model of the landslide. **b** The corresponding fragment network due to the presence of the rock discontinuities. Note: The logarithmic hue scale indicates the size of each fragment. Large fragments are represented by green to red colors whereas fine particles are given blue color

direction 120°), J_2 (dip 65°, dip direction 200°), and J_3 (dip 82°, dip direction 72°), subparallel to topography. J_1 and J_2 as lateral release surfaces of the instabilities have important effects on dissecting the rock mass into multi-shaped blocks. J_3 plays a fundamental role in contributing to initiation and development of shear planes. Because of the absence of infilling material in all discontinuities, the joints in a given zone are here defined by debonding particles along the joint plane with a 1.2-m thickness ($\approx$ the mean particle diameter). Here, all joint sets are created to be fully persistent and a certain amount of debonded particles will be dispersed in the joint gaps; therefore, the rock mass is altered with pre-existing joint sets and presented in the form of fragment network as shown in Fig. 5b.

Initial condition After the introduction of the joint sets, following the procedure suggested by Itasca (2014), the initial condition

is set by applying a gravitational acceleration vector of 9.81 m/s^2 in the negative y-direction. Then the model is cycled again to equilibrium under gravity loading to ensure initial steady-state condition is reached.

Boundary and loading condition The acceleration records from the 2008 Wenchuan earthquake are adopted as the input seismic loading. The criteria for selecting acceleration records are on the basis of two aspects. First, the seismological station should be located as close to the Wangjiayan landslide as possible; the second is that the seismic loading reflects the characteristics of the earthquake as much as possible. The 51MZQ station, called Mianzhu Qingping, is 49 km away from the location of Wangjiayan landslide and it has the shortest distance from the study area (Xu and Dong 2009). Furthermore, various studies (Song et al. 2017; Zhao and Crosta 2018) demonstrate that seismic data from this

station are accurate enough to reflect the effect of Wenchuan earthquake on related landslides. Based on the above, the seismic acceleration records at the 51MZQ station are used in this study to analyze Wangjiayan landslide.

The same seismic shaking duration of 100 s as Zhang et al. (2015) for analyzing Wenchuan earthquake induced landslide is also adopted in this study. According to the landslide profile direction of N76° E, the resultant seismic shaking in the horizontal direction starting from the EW (Fig. 6a) and NS (Fig. 6b) seismic components is calculated using Eq. (10) and presented in Fig. 6c, and the vertical acceleration is set as the UD component of seismic motion (Fig. 6e).

$$a_H = a_{E-W} \cdot \sin 76° + a_{N-S} \cdot \cos 76° \tag{10}$$

where a_H is the horizontal acceleration and a_{E-W} and a_{N-S} are the acceleration records in the east-west and north-south directions, respectively.

By integrations, baseline corrections, and band-pass filtering, the horizontal and vertical ground velocities is obtained as shown in Fig. 6d and f. The final step of the modeling process consists in employing the above obtained horizontal and vertical velocities along the absorbing boundary condition (Fig. 5) as base excitations using Eqs. (5) and (6). The angle of incidence of the seismic waves plays a fundamental role in the slope instability (Alfaro et al. 2012). However, in this study, not only the applied horizontal seismic velocity is obtained from the combined effect of EW and NS earthquake motions but the vertical seismic velocity (calculated from the UD component of the earthquake motion) is also taken into account to closely resemble earthquake loading (Martino et al. 2019).

Previous studies using DEM for analyzing earthquake-induced landslides have simplified the process that the slope shaking is synchronized along the failure plane in spite of varied slope topography (Tang et al. 2009; Wu et al. 2009a; Wu and Chen 2011). In fact, the seismic shaking wave reaching the predefined failure plane is non-synchronous due to the different elevations. Therefore, as presented in Fig. 5, the model corresponds to an earthquake source directly below the mountain, because the seismic wave is set to travel from the bedrock upwards into the slope mass. This makes numerical model can replicate the natural systems more accurately. In addition, the traveling velocities of P and S waves in this region is calculated using Eqs. (7) and (8) as 2,243 m/s (V_p) and 1222 m/s (V_s), which is in consistent with previously stated facts that relatively low P wave velocities near the ground surface were found in the area of the Longmenshan fault range consisting of mainly Quaternary deposits (Wu et al. 2009b).

Results and discussion

Dynamics of landslide motion

A visual presentation of the dynamic deformation process of the earthquake-induced Wangjiayan landslide is provided by selecting 9 distinct timestamps, as shown in Fig. 7. According to the figure, the slope failure occurs at about 7.1 s when tensile cracks initiate from the joint tip and propagate along the joint to the upper front region of the slope, corresponding to the location where the tensile stresses are concentrated. The failure initiates with disintegration of the slope material through the breakage of interparticle bonds, leading to loss of internal cohesion. In the meantime, the ground seismic shaking accelerations in two directions both begin to have relatively obvious fluctuations (Fig. 6). After the failure initiation, block sliding occurs when the coalescence is formed among the fractures in the rock bridges, the joints, and the tensile cracks that propagates to the slope surface. From 12 to 28 s, there is an abrupt change of ground motion, such that the cracks widened laterally and propagated vertically to the detachment surface, facilitating the subsequent downslope acceleration of landslide. As a result, the rock mass instantly begins to collapse into progressively smaller and more numerous joint-determined fragments as it travels down rapidly along the failure plane. Thus, rotation and collision are remarkable in the failure process, and some more rapid superficial movement and subsequent successive destabilizations at the sliding front are observed during the earthquake excitement (Fig. 7c–e). After about 28.5 s (Fig. 7d), the clustered fractures in the rear region of the lower portion of the slope, which corresponds to the topographic convexity, begins to propagate upward along the joint set, and grows to completion rapidly, leading to the separation of rock mass and the production of many fragments with relatively small sizes. The detached slope mass experiences intense interactions with the bedrock as the landslide collides onto the valley and continue to travel across the flat terrain at a high speed (Fig. 7d and e). The subsequent landslide propagation causes more damages to the slope mass, especially within the sliding front and topography change regions (transiting from topographic convexity to topographic concavity) as reflected by the gradual enlargement of damage zones. As the enlarged damage zone coalesce to completion from the failure plane to the internal slope mass (Fig. 7f and g), this enables the complete development of dynamic disintegration and dilatancy (controlled by pre-existing sub-vertical discontinuity sets J_1 and J_2) transforming the rock mass into a granular material promoting the full separation and whole movement along the sliding surface. Simultaneously, the collective motion works to stretch and thin the detached slope mass (Fig. 7i).

Disintegration process

The landslide starts out as a jointed rock mass that can disintegrate during transport. Disintegration process can be divided into two types (Pollet and Schneider 2004; Haug et al. 2016): (i) a primary (static), where the rock mass separates by breaking the rock bridges connecting fragments of competent rock (Eberhardt et al. 2004), and (ii) dynamic fragmentation where these particles are continuously reduced in size by grinding and comminution (Imre et al. 2010; Perinotto et al. 2015). This sequence of disintegration process can also be observed in this analysis, as shown in Fig. 8. It is worth mentioning that the same 9 timestamps used for deformation evolution of Fig. 7 is still applied here. Each joint-determined block in the source area is attributed a color that depends on its volume, expressed as the number of unit particles it contains (the hue scale in the figure is logarithmic). Before being released, the slope mass remains almost static and only elastic deformation occurs with very few bond breakages (Fig. 8a and b). Then, as the ground shaking intensity increases, bond breakages nucleate at the slope toe and cause instability from loosening rock blocks along the discontinuity (e.g., Fig. 8c at t = 20.43 s). Then, failure propagated upward to an upper region of the slope with
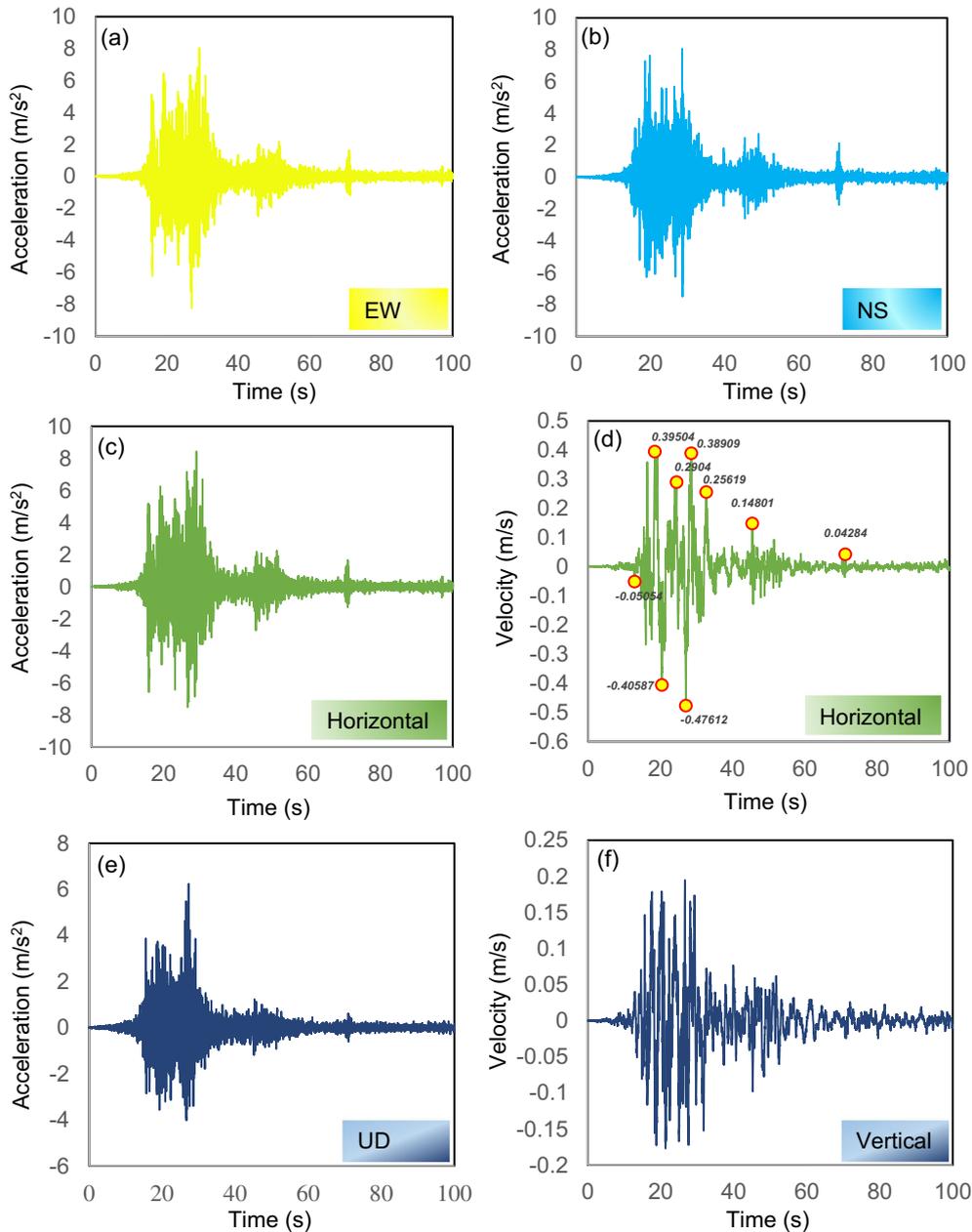
Fig. 6 Seismic time history curves: **a** EW acceleration; **b** NS acceleration; **c** horizontal acceleration; **d** horizontal velocity; **e** UD acceleration; **f** vertical velocity

further material disintegration and the rock block is then progressively fragmented, producing lots of small fragments in the frontal region (Fig. 8d and e). Concurrently, as the intensive seismic shakings proceed, the rock fracturing development progresses rapidly up to the slope crest, thus joint-bound rock material overlying the failure plane becomes detached, moves downward, runs out for some distance, and subsequently deposits downslope (Fig. 8f–i). Thus, the dynamic disintegration created by intensive shearing and dilatancy along the failure planes occurs (Pedrazzini et al. 2013; Wang et al. 2018), which is accompanied by progressive grain size reduction during the entire transport phase of the landslide.

Model validation
The dynamic disintegration processes accompanying transport of an earthquake-induced landslide have been delineated above. To further validate their accuracy and feasibility, close inspection of the final deposition topography as determined by the discrete element analysis is first compared with the actual post-failure landform. As manifested by the colored representation of the emplacement evolution (Fig. 7), rock blocks from the upper layers of the landslide experience longer runout distance than those near the basal shear surface and are not buried deeply in the depositional area. This dynamic characteristics accord well with the results obtained from continuum models, such as the smoothed
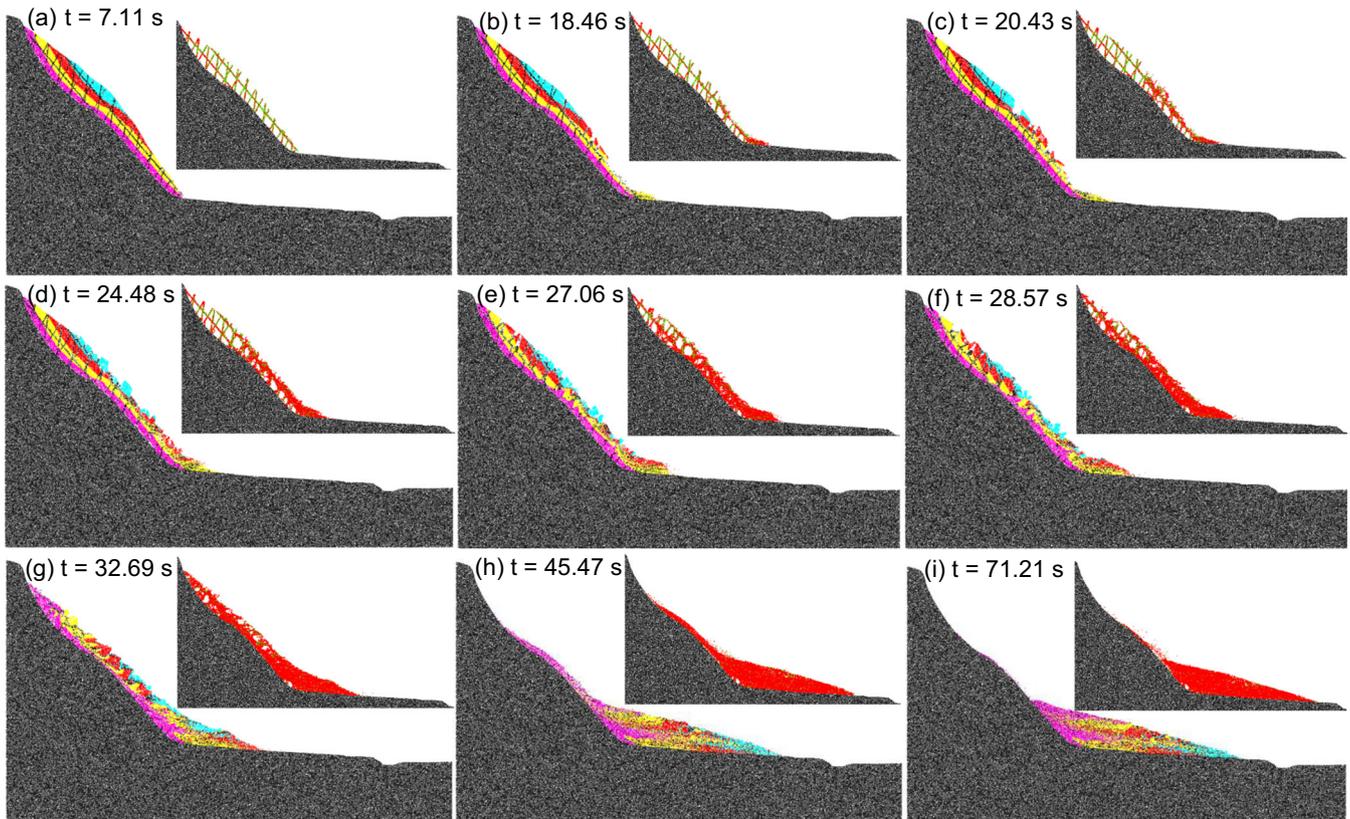
Fig. 7 The emplacement evolution of the Wangjiayan landslide at the selected timestamps: **a** 7.11 s; **b** 18.46 s; **c** 20.43 s; **d** 24.48 s; **e** 27.06 s; **f** 28.57 s; **g** 32.69 s; **h** 45.47 s; **i** 71.21 s. Note: The inset plot shows the details of crack distribution developed at the selected timestamps

particle hydrodynamics (Huang et al. 2012; Dai et al. 2014), the material point method (Li et al. 2016).

The final debris deposition shows that the major part of the slope mass has been intensely fragmented and only several large rock blocks are on the prevalence of finely crushed matrix material. The distribution pattern of the large rock blocks in the final disintegrated landslide deposit (Fig. 9a) matches well the field observations where the front and central parts contain large boulders and blocks, as shown in Fig 9b. Overall, the gradually decreased inclination angle of the final deposit from proximal to distal sections along the runout path coincides well with the site description. To be more precise, at the rear portion of the deposit, the dominance of fine debris marked by the blue color is consistent with field observation (Fig. 9c). In addition, the inclination angle within the rear part of the deposition based on the numerical simulation is found to be 33°, which is slightly smaller than 35° obtained from field investigation. The final runout distance (L_f in Fig. 9a) is found to be 337 m, which is quite consistent with the observed distance, i.e., 320 m. These findings can further confirm the credibility of the performed simulations.

Quantification of internal slope damage

A quantitative analysis of rock fragmentation during slope failure has been performed by recording the internal rock damage ratio (D_a) and computing the number of fine fragments over time. The fine fragments are those that have been reduced to a unit disk

particle and cannot be further split (Langlois et al. 2015). The rock damage ratio D_a is defined as the percentage of broken bonds occurring during the landslide over the total number of bonds at the initial static state, and the evolution of D_a can effectively characterize the progressive damage of a rock mass (Thornton et al. 1996). In the analyses, the ground shaking velocities in the vertical and the sliding directions are also plotted in Fig. 10a to illustrate the seismic-induced slope damage (Zhao and Crosta 2018). It can be observed in Fig. 10a that no damage occurs before 7.11 s (t_o) because of the very small intensity of seismic shaking. Between t_o and t_1 (16.8 s), the ground shaking intensity increases abruptly, particularly in the sliding direction. Thus, the percentage of slope damage in the layer *II* increases very rapidly with time, indicating that the fracturing initiated along the rock discontinuities with disintegration of the slope material through the breakage of interparticle bonds. This can be explained by that with the arrival of intense seismic shakings and the presence of the network of existing discontinuities, the slope mass is more susceptible to lose cohesions due to debonded grains being relatively unconstrained. As the intense earthquake ground motions continuously vibrates, joint-bounded intact rock strength was degraded as damage ratio accumulated fairly linearly until it reaches a relatively large value at t_2 (49.7 s). The subsequent sliding and impacting of fragmented rock blocks onto the valley floor during the landslide deposition can lead to further increase of D_a. During this process, layer *I* suffers the highest damage among the four layers due to the
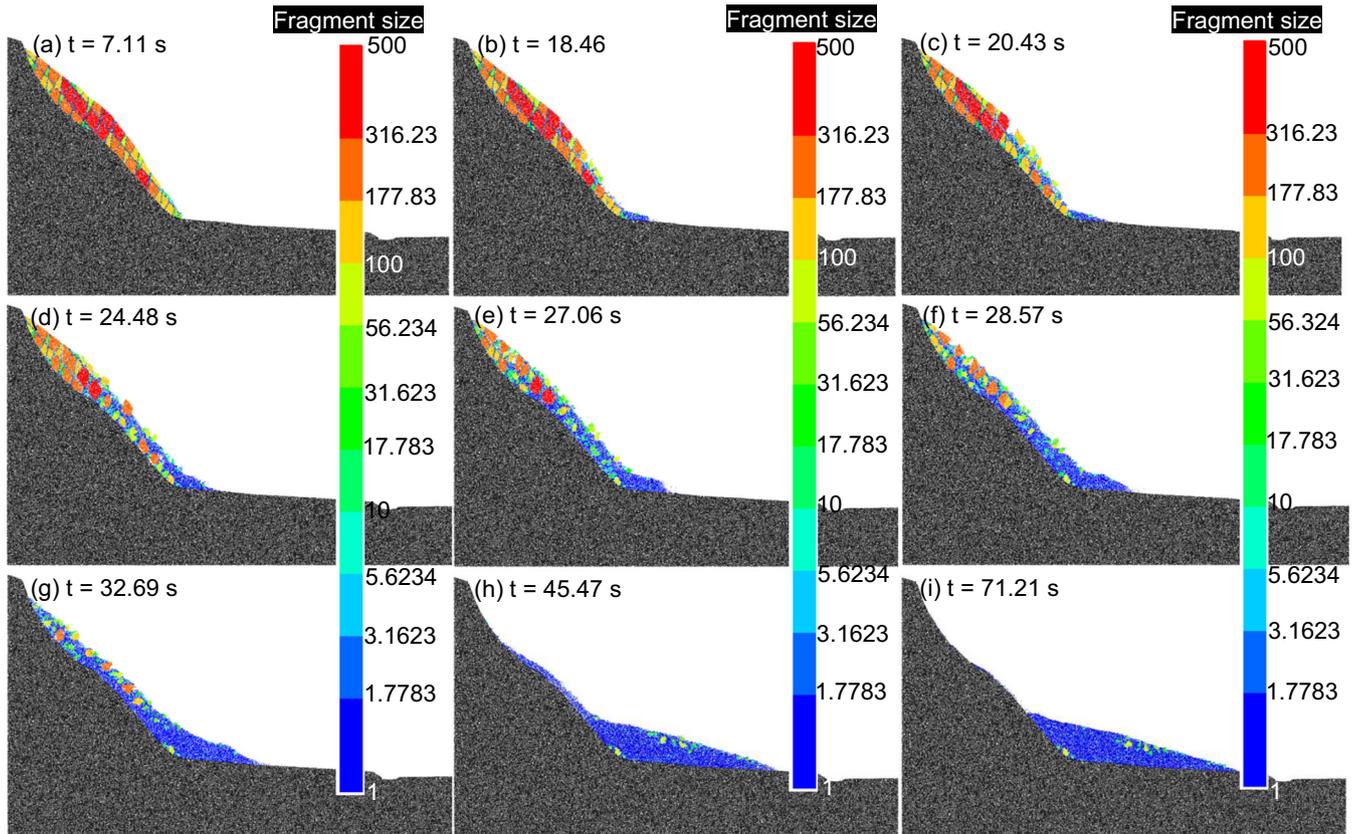
Fig. 8 The disintegration process of the Wangjiayan landslide at selected timestamps: **a** 7.11 s; **b** 18.46 s; **c** 20.43 s; **d** 24.48 s; **e** 27.06 s; **f** 28.57 s; **g** 32.69 s; **h** 45.47 s; **i** 71.21 s. Note: The logarithmic hue scale indicates the size of each fragment. Large fragments are represented by green to red colors whereas fine particles are given blue color

intense shearing with the bedrock. Layer *IV* also exhibits relatively high damage at the deposition stage, mainly because of its low strength and high compression loading near the ground surface. Middle layers *II* and *III*, in particular, layer *III* shows the smallest final rock damages, being constrained by the upper and lower layers. The final stable peak values of D_a, D_a-I, D_a-II, D_a-III, and D_a-IV are 70.0%, 75.0%, 66.5%, 68.9%, and 69.5%, respectively.

As stated by Langlois et al. (2015), the volume fraction of fine particles can provide a good quantitative assessment of the fragmentation dynamics in a landslide. The evolution of the volumetric fraction of the fine fragments is found to follow the same trend as the damage ratio (Fig. 10b). Before slope failure at time t_o (7.11 s), at relatively small ground shaking velocities, the volume fraction of fine fragments remains constant around 0.02 as a result of the debonded particles dispersing along the joint planes. As the ground shaking accelerates, an increase in finer fraction is found to reach around 0.07 at time t_1 (16.8 s), suggesting that the disintegration of the material starts immediately after the collapse. Then, as the intense seismic shakings last for a period to t_2 (49.7 s), the volume fraction of fine fragments increases at a much more quickening rate characterized by the rapid growth of cracks and obvious reduction of clast size. It should be noted that the runout is only 50% of its final value but 75% of the final number of fine fragments have already been produced at time around 32 s (Fig. 8i). Thus, disintegration obviously takes place in the course of

downslope ride. It is concordant with observations that the fragmented debris in the landslide deposits is consecutively reduced in grain size along the transport path, which has been reported in some well-documented numerical and field examples (Perinotto et al. 2015; Zhang et al. 2016).

Moreover, the growth rate of fragment number is then used to as an indicator to quantifying rock fragmentation intensity during the emplacement evolution of seismic-induced landslide. According to Figure 10b, the general variation of growth ratio of fragment number indicates that during landslide movement, the number of fragments has been reduced. After t_1 (16.8 s), as the seismic shakings remain at high intensity, propagating cracks could extend and coalesce with neighboring joints resulting in the development of a connected fragmented granular material along the failure plane, as reflected by the rapid growth rate of fragment number up to maximum at 27.5 s. This corresponds well with the horizontal seismic velocity reaching its maximum magnitude. Subsequently, multiple fractures grow continuously at many, closely spaced points, and persist accumulating as long as external input energy is available until the landslide loses momentum and deposits in the runout area. However, during the same period from t_1 to t_2 (49.7 s), the number of fragments declines rapidly. This phenomenon is expected as the fragmentation of the joint-bound rock mass produced a large amount of dispersed grains under the sustained intense seismic shakings, which leads to freshly broken
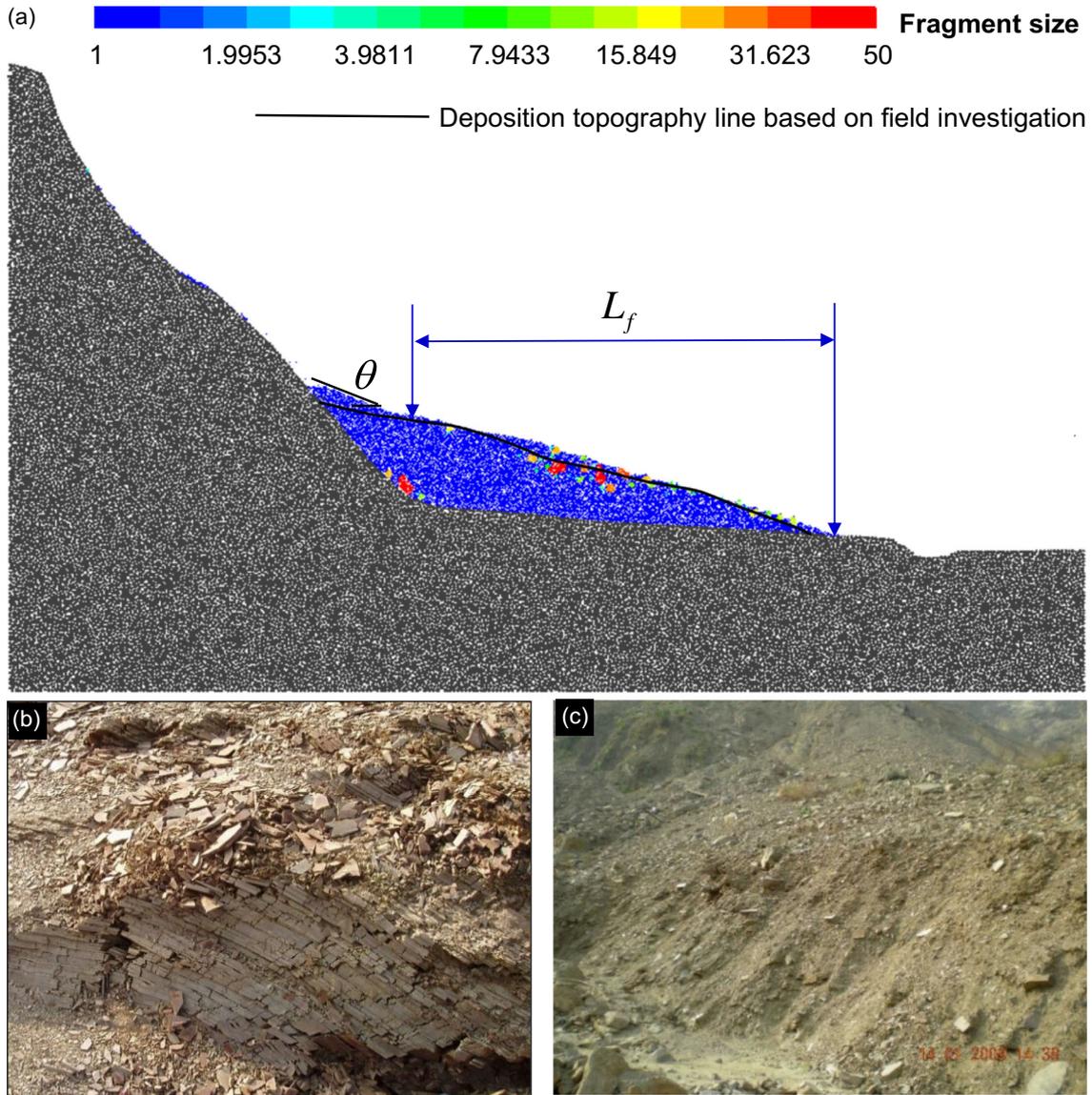
Fig. 9 Fragmented deposits following the Wangjiayan Landslide: **a** discrete element results; **b** large blocks that contain well-preserved original structure observed in the central and front parts of deposits; **c** large amounts of fine debris found in the rear part of deposit

fragments material progressively pulverized into fine-grained material. As a consequence, a decrease in the number of fragments can be observed. In addition, the prevalence of the fine-grained matrix can absorb a large portion of kinetic energy of the incoming rock fragments, which in turn preserves some relatively large boulder clusters.

Granular temperature and dispersive stress

During the high-speed motion of the sliding mass after detaching from the source area, particles along the basal layer exhibit high fluctuations due to the transformation of particle translational energy to vibrational energy. This induced a high collisional frequency between particles producing a strong impact pressure that easily exceeds the ultimate particle strength and induces a dynamic fragmentation with brittle features. Granular temperature in this context is proportional to the average value of the square of the grains' velocity fluctuations, with respect to their mean velocity (Zhou et al. 2016), and can be calculated as follows:

$$v_x^i(t)' = v_x^i(t) - \overline{v_x^i(t)} \tag{11}$$

$$v_y^i(t)' = v_y^i(t) - \overline{v_y^i(t)} \tag{12}$$

$$\omega^i(t)' = \omega^i(t) - \overline{\omega^i(t)} \tag{13}$$
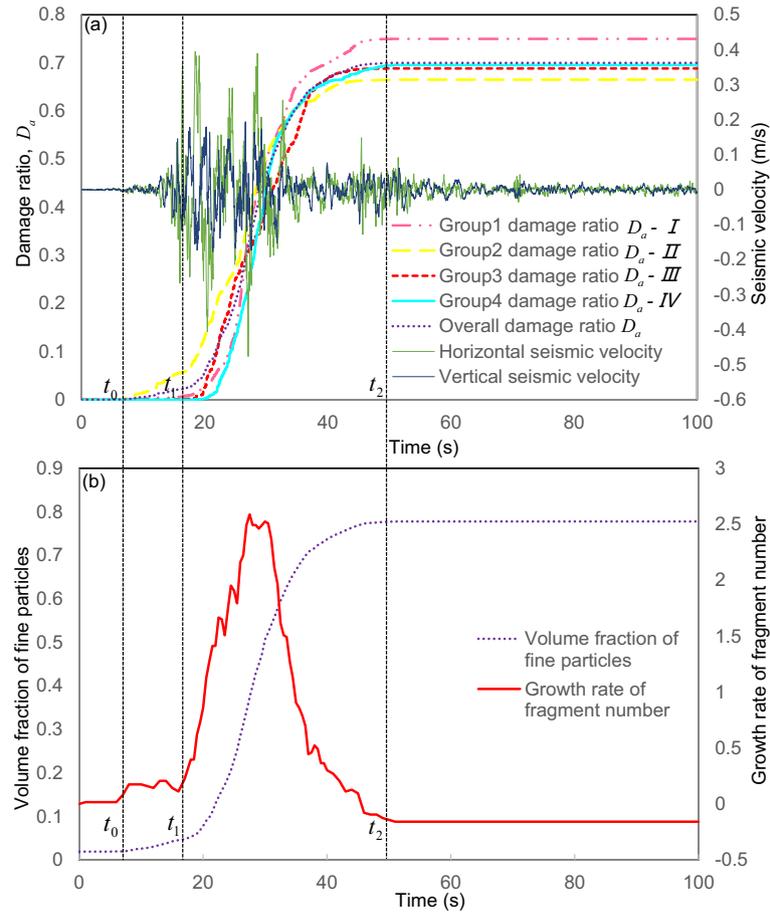
Fig. 10 **a** Evolution of rock damage in each slope layer and ground seismic shaking. **b** Evolution of volumetric fraction of fine fragments and growth rate of fragment number

where translational velocity components $v_x^i(t)$, $v_y^i(t)$ and angular velocity component $\omega^i(t)$ of the selected i-th particle in the granular ensemble can be divided into the mean velocity components $\overline{v_x^i(t)}$, $\overline{v_y^i(t)}$, and $\overline{\omega^i(t)}$ and fluctuating parts $v_x^i(t)'$, $v_y^i(t)'$, and $\omega^i(t)'$. The mean velocity components $\overline{v_x^i(t)}$, $\overline{v_y^i(t)}$, and $\overline{\omega^i(t)}$ can be attained by averaging the velocities of particles surrounding the selected i-th particle in the assembly of discrete solid mass.

Hence, the vibrational $T_V^i(t)$ and rotational $T_R^i(t)$ granular temperatures representing the intensity of particle exchange analogous to a thermodynamic temperature are calculated from the velocity fluctuations are expressed as follows:

$$T_V^i(t) = \frac{1}{2}\left[\left(v_x^i(t)'\right)^2 + \left(v_y^i(t)'\right)^2\right] \tag{14}$$

$$T_R^i(t) = \left(\omega^i(t)'\right)^2 \tag{15}$$

Moreover, by averaging $T_V^i(t)$ and $T_R^i(t)$ of all the particles composing the slope mass, the parameter $T_V(t)$ and $T_R(t)$ exhibiting the fluctuation intensity (degree of agitation) for the entire landslide is introduced:

$$T_V(t) = \frac{1}{N}\sum_{i=1}^{N} T_V^i(t) = \frac{1}{2N}\sum_{i=1}^{N}\left(v_x^i(t)'\right)^2 + \left(v_y^i(t)'\right)^2 \tag{16}$$

$$T_R(t) = \frac{1}{N}\sum_{i=1}^{N} T_R^i(t) = \frac{1}{N}\sum_{i=1}^{N}\left(\omega^i(t)'\right)^2 \tag{17}$$

Figure 11 illustrates the evolution of granular temperature for the entire granular system. It can be seen that after slope failure (t_o), both vibrational and rotational granular temperatures increase immediately with time. There is a slight increase of both temperatures between 7 and 16 s due to landslide acceleration. $T_V(t)$ and $T_R(t)$ reach the peak values of 63.1 and 12.0 m²/s², respectively, at around 35.02 s. Then, they both decrease gradually to nil when the bulk landslide mass gradually ceases motion after 70 s. According to the overall evolution of the granular temperatures for the entire granular system, five distinct timestamps are selected to show the distribution of $T_V^i(t)$ and $T_R^i(t)$ inside the granular body as presented in Fig. 12. At timestamp $t = 15.74$ s, the vibrational and rotation granular temperatures develop synchronously along the rock discontinuities because of their relatively

weaker rock structure and fewer restriction. As the seismic shakings proceed, there is an abrupt change of ground motion (see the seismic acceleration vectors and the horizontal and vertical velocity components in Fig. 6), such that more intense fracturing propagates and coalesce along the rock discontinuities accompanied with substantial release of fluctuation (e.g., Fig. 12c at 24.5 s). With development of more intense seismic shaking, cracks develop and grow to completion quickly along the basal failure plane, where it is composed of particles that, moving and colliding at high velocity, activate extensive fluctuations of vibrational and rotational granular temperatures (Fig. 12e and f). This observation indicates that during landslide propagation high granular temperature is generated in the basal layer where the intense shearing promotes the particle rearrangement characterized by vigorous particle agitation. This higher granular temperature implies more rapid particle exchange and higher rates of particle collisions. However, the coarse fragments on the free surface are passively carried by neighboring fine-grained particles and are barely collision dominant, with the enhancement of granular temperature and fluctuation rarely observed. With the subsequent sliding and impacting of detached slope mass onto the valley floor during the landslide deposition, the granular temperatures possess relatively large values near the front and rear regions and quickly dissipates towards the interior of the accumulated deposit. This phenomenon is explained by the fact that particles in the rear region that are still falling down the slope transfer their momentum by pushing the deposit forward, and therefore frontal slope mass becomes even more collision dominant with collisions on the free surface enhanced under little constraint. After the intense seismic shaking period, the particles in the accumulated deposit therefore exhibit a gradually attenuating fluctuation intensity. This phenomenon accords well with the statement that the granular temperature can be dissipated or vanished rapidly due to interparticle collisions when external energy stops (Campbell 1990).

As stated by Wang et al. (2015), particle fragmentation caused by frequent intensive collisions will occur as the increase of granular temperature accumulated in particles; at the same time, this process can result in the generation of dispersive stresses, which can further dilate and disperse the detached slope material (Davies et al. 1999), facilitating the occurrence of fragmentation and leading to a farther movement of the avalanche. Hence, the deviator stress q' introduced by Imre (2010) is calculated to quantify the dispersed state and analyze the influence of fragmentation on the emplacement of landslides, which is shown below:

$$q' = \frac{1}{\sqrt{2}} \left[\left(\sigma'_{1,f} - \sigma'_{2,f} \right)^2 \right]^{1/2} \tag{18}$$

The input average normal and shear stress tensor $\overline{\sigma}_{ij}^{(P)}$ of a particle (p) is calculated as

$$\overline{\sigma}_{ij}^{(P)} = \frac{1}{V^{(P)}} \sum_{N_c} \left| x_i^{(c)} - x_i^{(p)} \right| \cdot n_i^{(c,p)} \cdot F_j^{(c)} t_f \tag{19}$$

where V is the volume of the particle, N_c is the number of particle/particle or particle/ground contacts acting on (p), $x_i^{(p)}$ and $x_i^{(c)}$ are the locations of the particle centroid and its contacts, $n_i^{(c,p)}$ is the unit normal vector directed from a particle centroid to its contact location, and $F_j^{(c)}$ is the force acting at a contact. The magnitudes and the directions of the principal stresses $\sigma'_{1,f}$ and $\sigma'_{2,f}$ of particles undergoing fragmentation are calculated from Eq. (19) as the eigenvalues and eigenvectors of the stress tensor $\overline{\sigma}_{ij}^{(P)}$.

Figure 13a illustrates the variation of q' over time during the landslide simulation. According to the figure, it can be seen that from 0 to 4.6 s, q' fluctuates slightly around a constant value of 1.7 MPa due to seismic shaking. Then, it fluctuates abruptly from 1.7 to 0.9 MPa during a short period of time near $t_o = 7.11$ s before the slope failure. As the ground shaking accelerates, the rock bridges break intermittently and the cracks grow steadily within the detached slope mass, resulting in a significant increase of dispersive stress with increased fluctuation intensity. The value of q' reaches high value of 10.95 MPa at 16.5 s as the slope mass descends from its in situ position and experiences temporary relief when frictional bonds along the pre-existing discontinuities are progressively overcome. As the ground continuously vibrates, the deviator stress q' reaches its maximum of 16.8 MPa at 22.7 s and experiences wild fluctuations in the subsequent landslide propagation, immediately following rock mass break-up with relatively minor fragmentation as the sliding body evolves from block sliding with a finite increment of landslide motion to more dynamic fragmented flows. A rock mass subject to such stress fluctuations will be more readily fractured and therefore latter development of the stress variation with increased fluctuation intensity may promote the development of fragmented or fine-grained basal shearing layer. Furthermore, it results in an increasing proportion matrix to blocks with displacement in response to progressive dynamic disintegration of an increasing number of finer grains. As illustrated in Fig. 13c and d, at time of $t = 16.5$ s and $t = 22.7$ s, when the deviator stress q' reach the 11.0 MPa, and 16.8 MPa (highest), respectively, the relative velocities between the particles are so high that stresses sufficient to yield fragmentation occur. Particles colored in blue indicate a practically stress free, dispersed zone of the assembly where all particles are fracturing, collapsing, and dilating as it does so into a loose granular mass (Fig. 13d). With the presence of particle dilation and enhancement of particle fluctuation during the intense shaking period, the intensity of particle collisions will be strengthened by increasing a relative velocity and induce the occurrence of intense dynamic fragmentation. This phenomenon illustrates clearly that during the extremely rapid motion of the sliding mass, a strongly sheared and agitated layer spontaneously appears representing a highly dynamic collisional granular regime. Correspondingly, a dispersive pressure is generated with the occurrence of a locally high dilation and supports a relatively sparse packing of grains moving as a whole, which is well in accordance with dynamic fragmentation hypotheses (Davies 1982; Taberlet et al. 2007; Wang et al. 2015). In the highly dispersed state, indicated by the blue coloring of the particles (Fig. 13e), the generation of a dispersive stress due to fragmentation also can further dilate and disperse the particle assembly, further facilitating the occurrence of dynamic disintegration. After $t_1 = 71.2$ s, q' remains relatively small (≈ 0.32 MPa) and then slightly dropped to 0.28 MPa at $t = 100$ s (Fig. 13f and g), because the slope mass has arrived at a low-speed deposition state and readjust to accommodate much of the deformation taking place in the sliding body during emplacement, and allowing itself organizing into a steady flow across the horizontal runout valley.
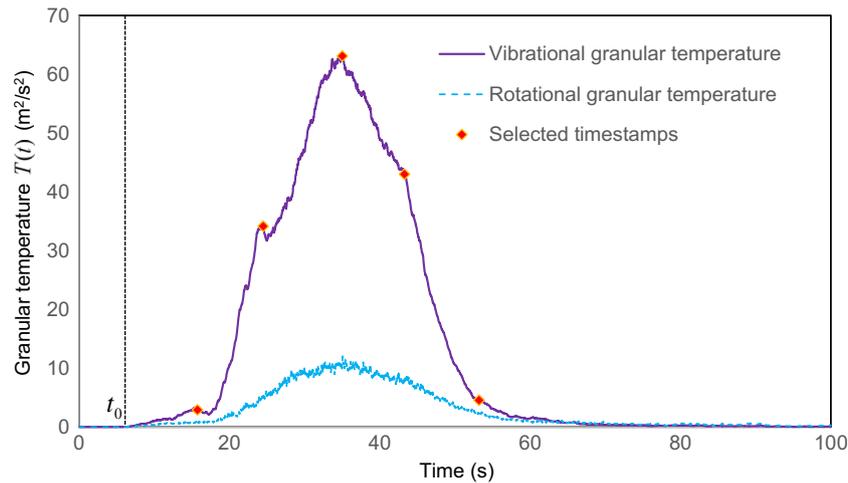
Fig. 11 Evolution of the vibrational (T_V) and rotational (T_R) granular temperatures within the translating slope mass

Morphology and structure of fragmented deposits

Intense earthquake loadings cause cross-cutting fractures to be nucleated in different, closely spaced parts of the slope material nearly simultaneously, subsequently growing and merging leads to instantaneous fragmentation and pulverization of the solid during the rapid landslide propagation and deposition. This catastrophic process appears chaotic and unpredictable. However, out of the randomness, the mass distribution of fragments $p(m)$ as the most important characteristic quantity of the fragmenting system is found to exhibit a power law behavior:

$$p(m) \sim m^{-\tau} \tag{20}$$

where $p(m)$ is the probability of finding a fragment of mass within a tolerance of increment dm. The value of the exponent τ is mainly determined by the dimensionality of the fragmenting system (Åstrom et al. 2004; Ma et al. 2018) and by the brittle and ductile characteristics of the mechanical response of the material (Levy et al. 2010; Timár et al. 2010).

To obtain the fragment mass distribution, the characteristic fragment size is defined as (Zhao et al. 2018):

$$d = \sqrt{V_f/V_o} \tag{21}$$

where V_f is the volume of a fragment (calculated as the total volume of particles in the fragment) and V_o is the volume of the sample.

In addition to the fragment mass distribution defined in Eq. (20), a fractal distribution is given by the relationship between the fragment number and size:

$$N(d > d_i) = C d_i^{-D} \tag{22}$$

where $N(d > d_i)$ is the number of fragments with size greater than a certain size d_i, C is the number of elements at a unit length scale, and D is the fractal dimension.

However, it is very difficult to accurately estimate the total number of fragments. Moreover, the N value calculations are typically unavailable from the conventional size distribution (Xu et al. 2013). Hou et al. (2015) estimated the fractal dimension using the Gates-Gaudin-Schuhmann (GGS) distribution based on the following expression:

$$M(d < d_i)/M_T = (d_i/d_{max})^n \tag{23}$$

where $M(d < d_i)$ is the cumulative mass of particles smaller than d_i, M_T is the total mass of all of the fragments, and d_{max} is the size of the largest fragment.

A natural logarithm transformation is applied for both sides of Eq. (23), and the fractal dimension can be calculated as:

$$\ln[M(d < d_i)/M_T] = n^* \ln(d_i/d_{max}) \tag{24}$$

where n is the GGS distribution parameter representing the slope of the fitting line in the coordinate system of $\ln[M(d < d_i)/M_T] \sim \ln(d_i/d_{max})$.

Based on simple mathematical derivations, Turcotte (1986) found that the power law distribution defined in Eq. (20) is equivalent to the fractal distribution defined in Eq. (22), and their exponents have a relationship $D = 3(\tau - 1)$. The GGS distribution is also equivalent to the fractal distribution with $D = 3 - n$.

The fragment mass distributions of the initial static and final deposition states are presented in Fig. 14a. It can be observed that magnitude of exponent value $\tau = 1 + D/3$ of the power law approximation for fragment mass distributions increases significantly from 1.09 at initial static state to 1.6 at final deposition state. The higher the value of D, the more graded the particle size distribution and the larger the number of fine particles will be (Crosta et al. 2007). Therefore, the obtained fractal dimension $D = 3(\tau - 1)$ increases sharply from 0.27 to 1.8, indicating the severe grain crushing and comminution occurring within the translating joint-bound rock mass. Moreover, as shown in Fig. 14b, the slope of the fitting straight line $n = 3 - D$ decreases after the cessation of earthquake ground motions. As a result, fractal dimension D increases with comminution time and with the increased
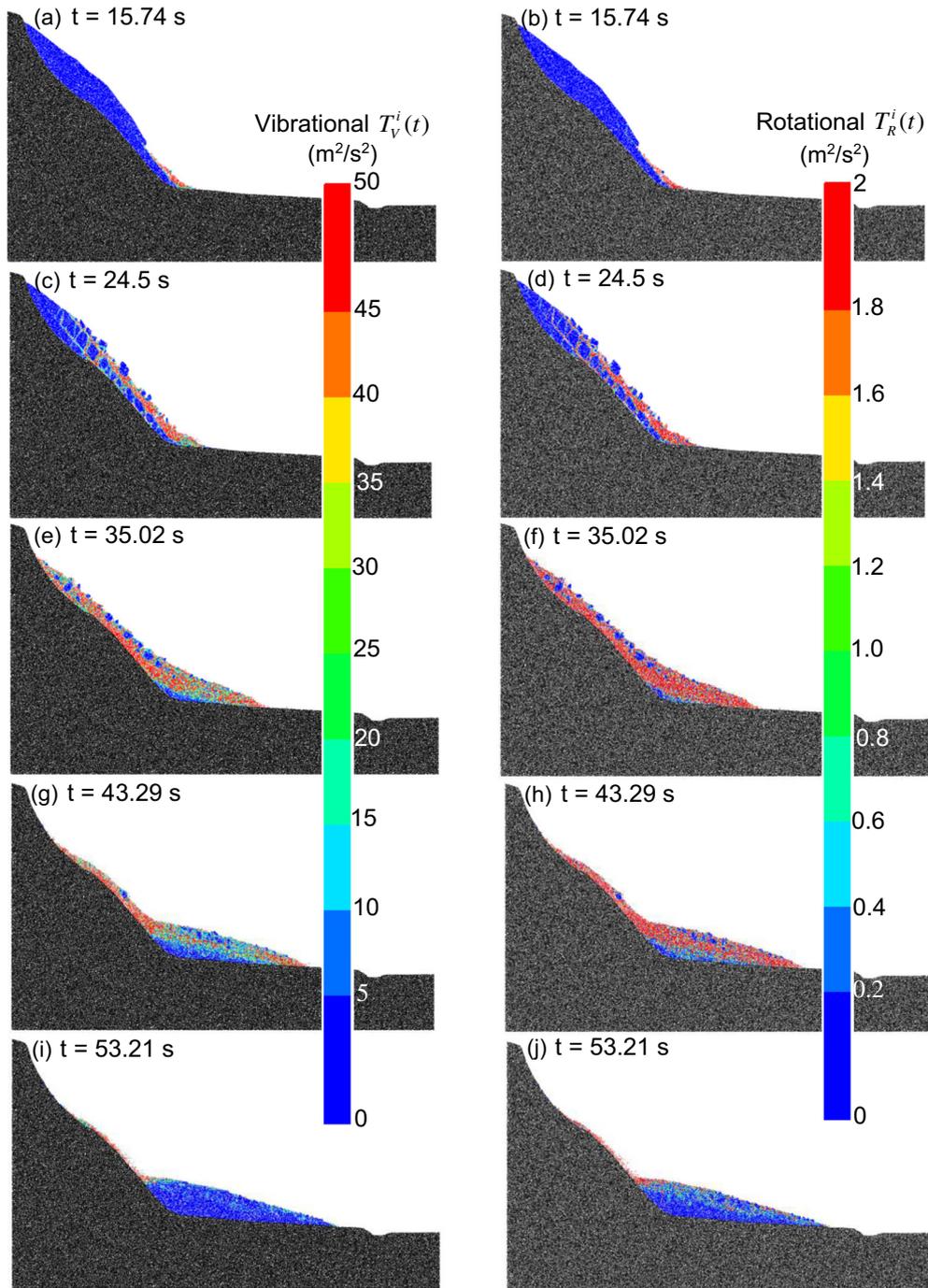
Fig. 12 The distribution of granular temperatures within the Wangjiayan landslide at the selected timestamps: **a**, **b** 15.74 s; **c**, **d** 24.5 s; **e**, **f** 35.02 s; **g**, **h** 43.29 s; **i**, **j** 53.21 s

production of fines, revealing that larger fragments are segmented along the well spatially distributed pre-existing rock discontinuities owing to the propagation of seismic waves, and fully developed fractures and fine debris are produced after the 100-s duration of seismic shaking, thus leading to higher values of D. The measured D of 0.25 and 1.73 at initial static and final deposition states are close to the fractal dimension value of 0.27 and 1.8

by calculating the exponent of power law approximation for fragment mass distribution. It reflects that the calculated fractal dimension can be validated as a convincing descriptor in fragmentation characteristics for its physical soundness and mathematical rigor, though the obtained fractal dimension from DE simulation is slightly lower than measured fractal dimension of real landslides deposits (Crosta et al. 2007). This is attributed to
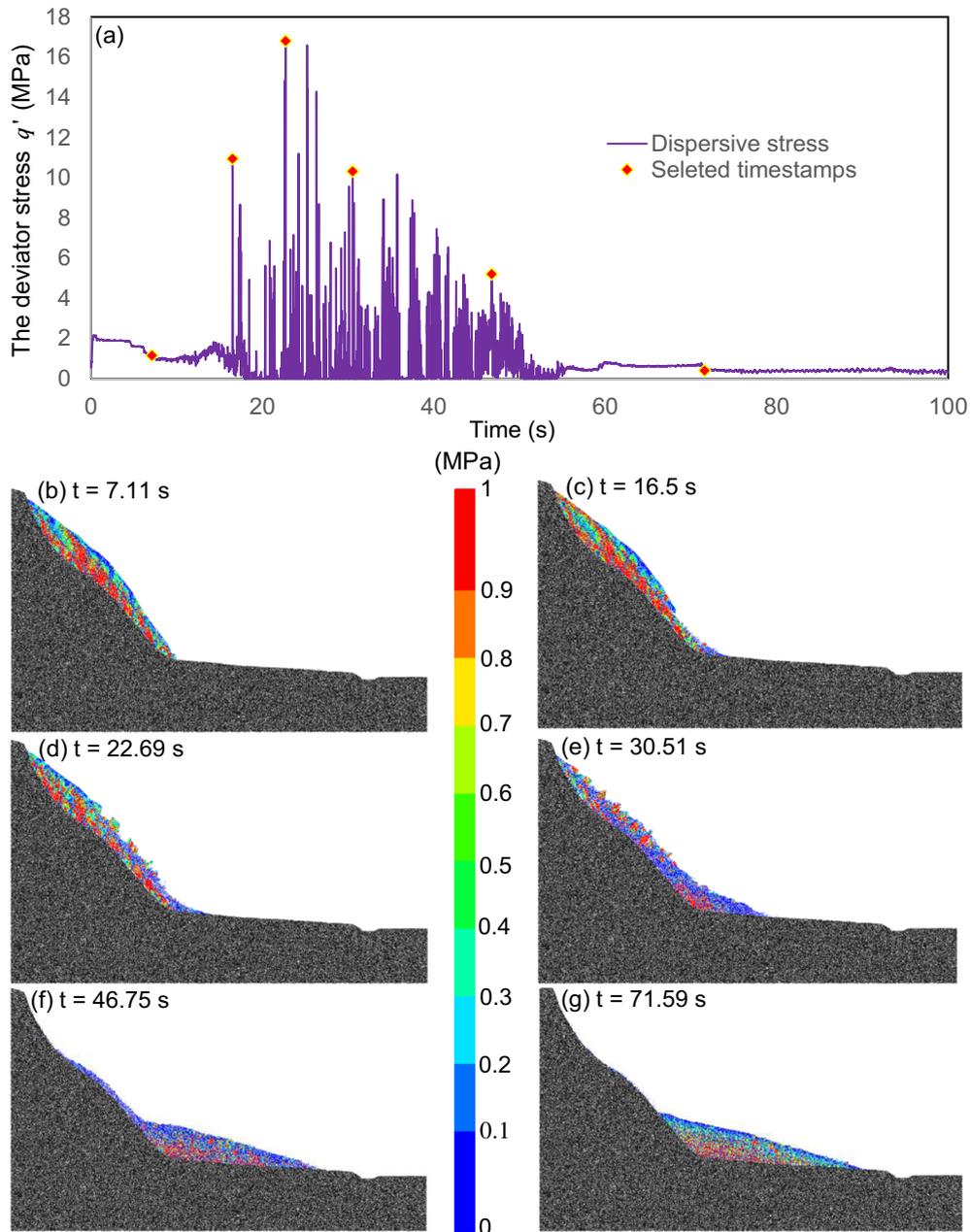
Fig. 13 a Variations of the deviator stress of the Wangjiayan landslide; the distribution of the deviator stress within the landslide at the selected timestamps: **b** 7.11 s; **c** 16.5 s; **d** 22.69 s; **e** 30.51 s; **f** 46.75 s; **g** 71.59 s

the nature of distinct element that does not allow the dispersed disk grains to be further disaggregated. However, it still can qualitatively demonstrate that the sliding rock mass consecutively experienced an obvious reduction in grain size along the transport path.

The sedimentary fabric and depositional features can be tracked via cumulative fragment size distribution to acquire a deep knowledge of the dynamic disintegration process within the landslide emplacement in response to the seismic shakings. Figure 14c illustrates the fragment size distribution obtained for jointed rock blocks before (hollowed symbols) and after (solid symbols) seismic loading. Close examination of fragment size distribution reveals that at the initial static state before the arrival of seismic waves, the jointed rock mass consists of a large number of coarse fragments of varied sizes ($d > 0.07$, $P > 94\%$). At the end of the seismic motion, a large quantity of fine-sized fragments is generated, leading the fragment size distribution to shift leftward to the fine size range ($d \leq 0.07$, $P > 90\%$). The initial and final fragment size distributions can be fitted well by a Weibull's distribution function. This distribution, which is equivalent to the Rosin-Rammler distribution, has successfully provided a good description of the simulated fragment size distribution (Shen et al. 2017;
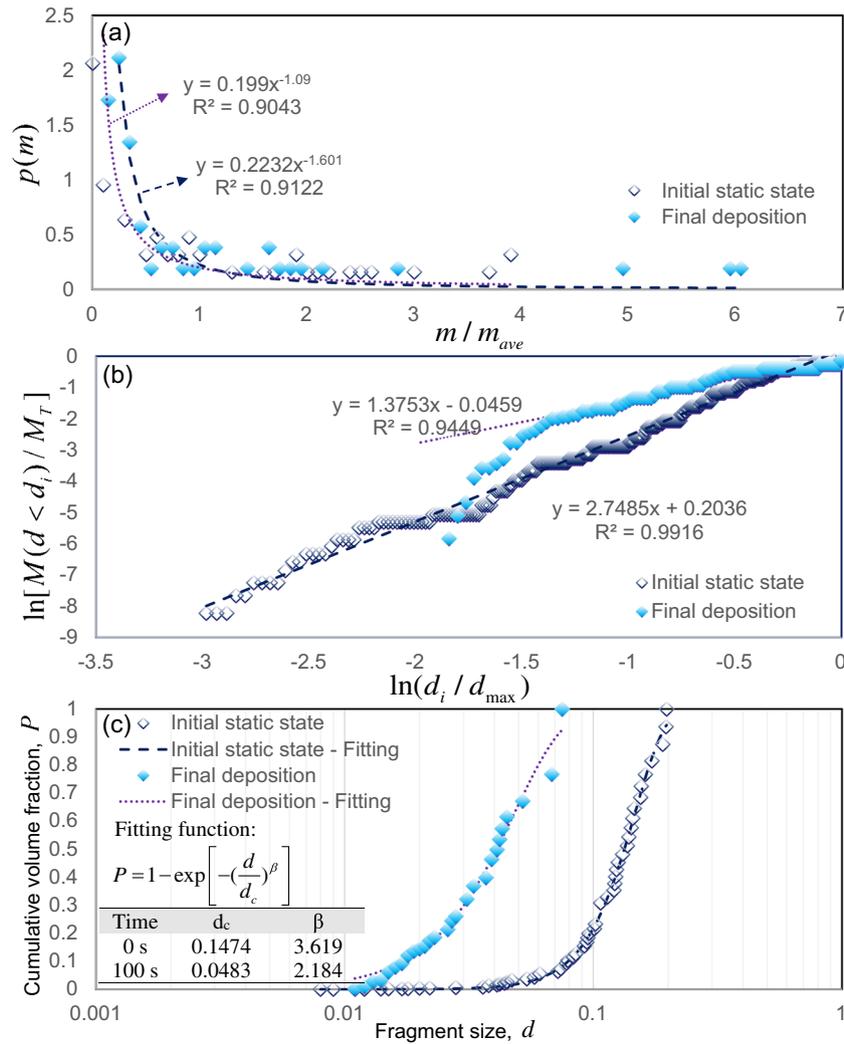
Fig. 14 **a** Mass distribution of fragments using the power law distribution. **b** Mass distribution of fragments using the Gates–Gaudin–Schuhmann distribution. **c** Volume-based size distributions of fragments. Note: Numerical results are represented by the scattered data points and fitted distributions are represented by lines

Ma et al. 2017). The two-parameter Weibull distribution can be expressed as

$$P = 1 - \exp\left[-\left(\frac{d}{d_c}\right)^{\beta}\right] \quad (25)$$

where d_c and β are fitting parameters. d_c is an index to quantify the level of fines in the fragmenting system. A low d_c value is expected if the fragmenting system consists of a high level of fines. The parameter β is a measure of the spread of the fragment size distribution, where the distribution is narrower for a larger value of β.

Significant decreases in parameters d_c (from 0.15 to 0.05) and β (from 3.6 to 2.2) can be observed (Fig. 14c) from initial static state to the final deposition after the end of earthquake motions. It reflects that a severe rock fragmentation intensity within the translating slope mass occurs under the strong earthquake ground motion; a large number of fine particles is produced, characterized by a more graded and wider particle size distribution.

Further insights into the disintegrated slope mass at the final deposition can be acquired by exploring the features of the fragment-size statistics; therefore, a statistical analysis is performed to examine the characteristics of fragment populations of the landslide deposit. It can be observed in Fig. 15a that the distribution of nominal fragment sizes for the landslide deposit is asymmetric, being skewed towards the smaller sizes. Such a distribution lends itself to approximation of a log-normal distribution (Fityus et al. 2013). The cumulative distribution and probability density functions of the log-normal distribution are expressed by Eqs. (26) and (27), respectively:

$$F_X(x) = \frac{1}{2} + \frac{1}{2} erf\left[\frac{\ln(x) - \mu}{\sqrt{2}\sigma_{SD}}\right] \quad (26)$$

$$f_X(x) = \frac{1}{\sigma_{SD}\sqrt{2\pi}x} e^{-(\ln x - \mu)^2/2\sigma_{SD}^2} \quad (27)$$

where *erf* is the complementary error function, σ_{SD} (the standard deviation of $\ln(x)$) is the shape parameter which affects the general

shape of the distribution, and μ (the mean of $\ln(x)$) is the location parameter that controls the location on the x-axis.

As demonstrated in Fig. 15a, the nominal fragment size follows a lognormal distribution. Most of deposited fragments sizes distribute within a nominal fragment size range ($0.01 < d \leq 0.015$) being dominant around 33% in total, inferring a dynamic disintegration of the slope mass occurs continuously during the landslide transport. In addition, the lognormal quantile-quantile (Q-Q) analysis is applied to evaluate how well the distribution of fragment sizes matches a lognormal distribution and to better interpret fragment size statistics (inset plot in Fig. 15a). It can be observed from (Q-Q plot) that the distributions are fluctuating at coarse fragment size range, indicating the presence of large unbroken blocks.

In advance of more detailed investigation on the mechanisms operating during the transport of an earthquake-induced landslide, a statistical analysis is put forward to examine the shape characteristics of fragment populations by checking the fragment shape isotropy. The shape isotropy can be calculated using the square root of the ratio of the larger I_1 and smaller I_2 eigenvalues of the tensor inertia of the 2D fragment shape (Timár et al. 2010). The tensor inertia can be calculated as follows:

$$I_{ij}^{fragment} = \sum_{d=1}^{N_d} \left(I_{ij}^d \delta_{ij} + m^d x_i^d x_j^d \right) \tag{28}$$

where the fragment contains N_d base disks, each with mass m^d, and inertial tensor $\mathbf{I}^d$ relative to the disk local Cartesian axis, and δ_{ij} is the Kronecker delta. The vector $\mathbf{x}^d$ is given by $x_j^d - x_j^{fragment}$, where $\mathbf{x}^d$ and $\mathbf{x}^{fragment}$ are the vectors describing the constituent disk and fragment centroids respectively.

The mean and standard deviation of $\sqrt{I_1/I_2}$ is found to be 1.29 and 0.25, respectively, with a coefficient of variation (C_v) of 0.195 for the landslide deposit (Fig. 15b). The $C_v < 1$ is known as a relatively low variation, indicating a high level of fragment shape isotropy. It is interesting to note that although the fragment shape isotropy of the deposition is relatively high, an obvious deviation from the mean value of $\sqrt{I_1/I_2}$ is found in the larger fragment size. This is expected because coarse blocks have not undergone any further textual maturation, such as friction abrasion, continuous comminution, and grinding, which promotes the fact that particles are more mature with higher rounding and smoothness (Perinotto et al. 2015). Similar behavior was also observed in other reported large-scale landslides (e.g., Crosta et al. 2004; Zhang et al. 2011).

Fragmentation degree and landslide runout

As discussed in the previous sections, a set of rock properties has been employed in a preliminary numerical investigation of the Wangjiayan landslide. The obtained numerical results reveal the dynamic disintegration and emplacement mechanism of landslide during earthquake loadings. To generalize this research, a systematic parametric study on the influence of rock strength on slope damage, dynamic runout, and fragmented deposition has also been performed. In testing the effect of rock strength, the same pattern of rock discontinuities is kept, while the bonding strength of particles is

varied from 11 to 36 MPa with an increasing step of 5 MPa. Figure 16 compares the distribution of final slope damage and the sedimentary fabric within the deposit for tests on rock slopes with various strengths. It can be seen that when the rock strength increases, the surface of the deposit becomes less smooth with larger irregularities. It is worth noting that regardless of the rock strength, the internal structure of the deposit experience significant disturbance with the emergence of rock material from the inner layers can be observed at the surface. Consistent with previous observations, the final deposits consist of rafted large blocks laying on matrix of fine-grained material (Wang et al. 2018). Although large blocks are found at the surface of the deposit, their distribution remains very heterogeneous and the size of outcropping blocks can vary significantly. For bonding strengths $\overline{\sigma}_c = 11$ MPa and 36 MPa, the largest fragment sizes are 0.076 and 0.153, respectively. This is in good agreement with the observations made at the surface of natural events (Wang et al. 2018).

In order to precisely identify the effect of bonding strength ($\overline{\sigma}_c$) on the dynamic runouts of the earthquake-induced landslide, the degree of fragmentation F_D is used to provide a measure for the damage that the material has experienced (Haug et al. 2016), which is calculated as $F_D = \frac{M_{max}}{m_{max}}$ with M_{max} and m_{max} being the mass of the largest fragment at initial static state and final deposition, respectively.

The degree of fragmentation (F_D) observed in the numerical simulations for varying bonding strength ($\overline{\sigma}_c$) is plotted in Fig. 17a. It is found that F_D drops drastically as $\overline{\sigma}_c$ increases to 31 MPa and then slightly increases as $\overline{\sigma}_c$ reaches 36 MPa. However, the overall slope damage ratio decreases exponentially with the increase in particle bonding strength. The numerical results are also analyzed with respect to the mobility of the rock mass in Fig. 17b, where the travel distance of the center of the sliding mass (L) and travel length of the front of the deposits (L_f) is plotted with respect to the degree of fragmentation (F_D). The distance L can be obtained using equation (29) and L_f is defined as the horizontal distance of the slope mass' initial front position and the front of the final deposits.

$$L = \sum_{i=1}^{N} m l_i / M_{sum} \tag{29}$$

where M_{sum} being the sum of the mass of all particles and l_i is the spreading distance of particle i.

As the degree of fragmentation is dimensionless, the travel distance can be set as dimensionless relative to its own size, which is defined using the square root of the area of the rock material. It can be seen in Fig. 17b that the distance traveled by the front of the landslide shows an increase with the increase in the degrees of fragmentation. The front is also observed to be strongly affected by the degree of fragmentation below $F_D \approx 5$. For degree of fragmentation above this value, displacement of the front of the deposits seems to reach saturation. This finding can well match the scaled analogue physical models in Bowman et al. (2012) with respect to the dynamic disintegration of intact and jointed rock blocks and the well-documented field observations in Legros
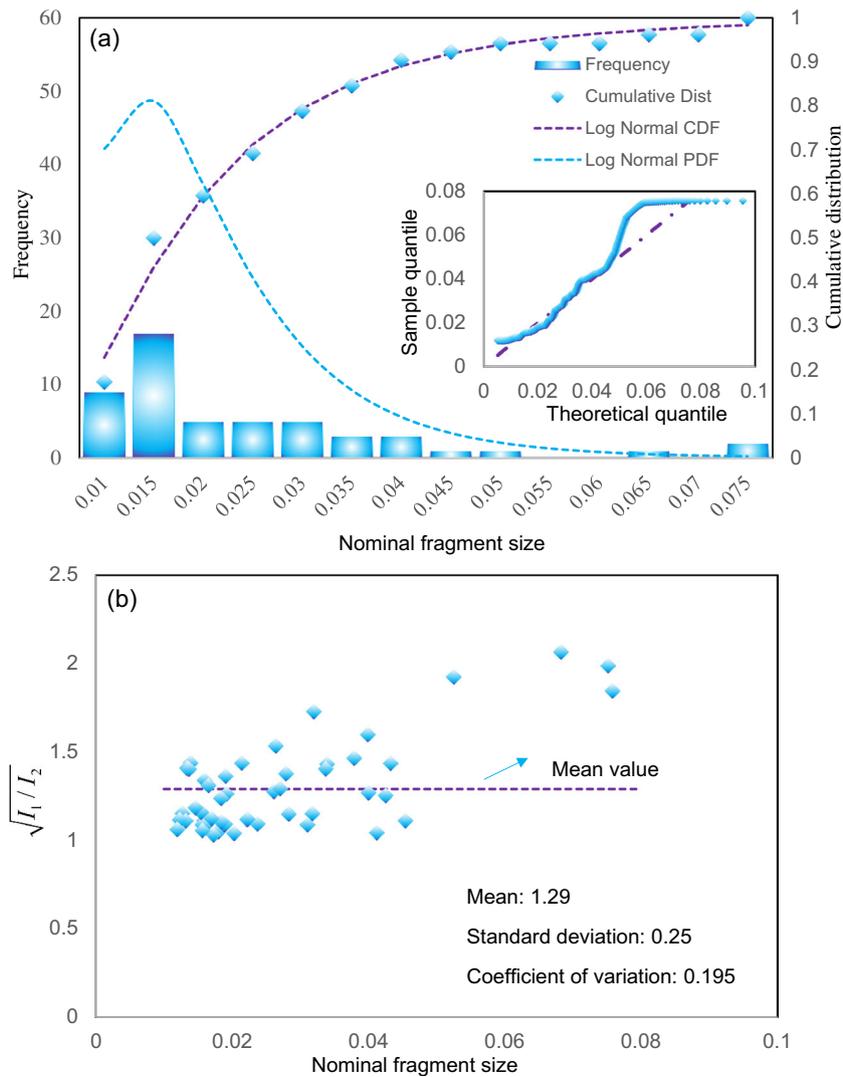
Fig. 15 **a** Fragment size frequency distributions of the deposit with corresponding log-normal approximations. **b** Distributions of the square root of the ratio of the larger and smaller eigenvalues of the tensor inertia of the fragment shape for checking shape isotropy of the deposit

(2002). It is worth noting that the travel distance of center mass follows a similar trend but with a milder increasing rate and an earlier saturation state for F_D. This can be explained by the sliding front that experiences intense interactions with the bedrock during the landslide propagation and deposition, allowing it to attain a higher energy as the main driver for fragmenting the rock mass and promoting long runout. According to Fig. 17, the numerical results (i.e., F_D, L_f, and L) can be well fitted by exponential functions of the form:

$$Y = C_1\left(1 - e^{-C_2(F_D - 1)}\right) \tag{30}$$

where Y is the dependent variable (L_f and L), C_1 and C_2 are the fitting constants, and F_D is the degree of fragmentation.

Conclusions

To understand the role of rock fragmentation and transport mechanism in earthquake-induced landslide at the macroscopic and microscopic levels, the processes of rock slope failure, runout, and deposition were investigated using 2D DEM. The following conclusions are drawn as follows:

(a) The dynamic response of the investigated slope to earthquake shaking is numerically evaluated focusing on crack initiation, propagation, and coalescence within the jointed rock mass. The internal slope fragmentation is quantified by examining the continuous increase of rock damage ratio and volume fraction of the generated fine particles.

(b) During the mass transport process, the slope is fragmented progressively due to intense shearing, allowing a basal layer of fine particles to be generated with simultaneous occurrence of violent interparticle collisions, increase in rotational
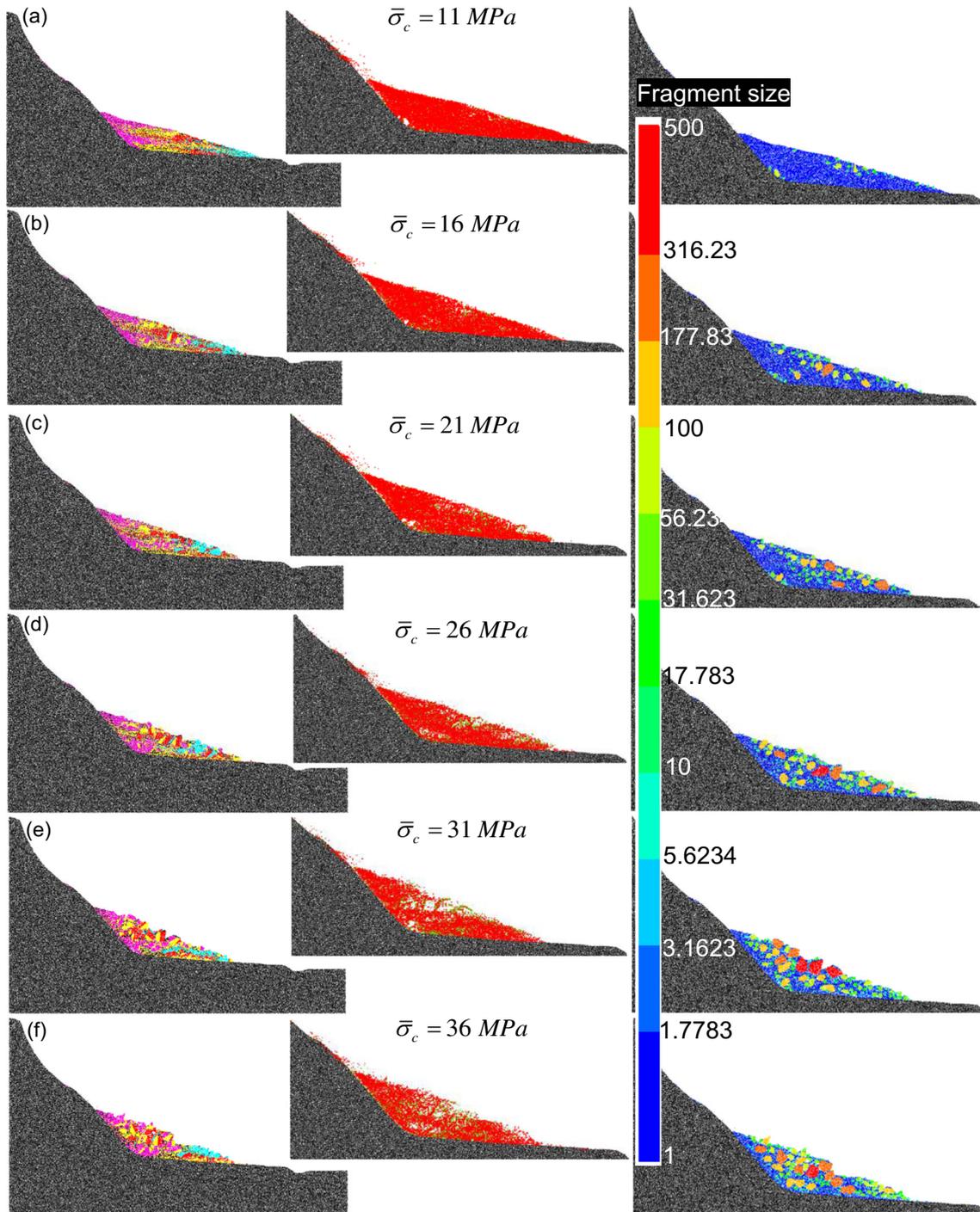
Fig. 16. Numerical investigation of final landslide deposit for tests with various particle bonding strengths: **a** 11 MPa, **b** 16 MPa, **c** 21 MPa, **d** 26 MPa, **e** 31 MPa, **f** 36 MPa. The left column denotes distribution of slope mass, the medium column presents distribution of slope internal damage, and the right column depicts distribution of fragment size in the final landslide deposits, respectively

and vibrational granular temperatures, and vibration-induced dilatation.

(c) Characteristics of fragmentation are systematically analyzed in terms of the statistics of the fragment mass, fragment size, and fractal dimension, revealing that dynamic disintegration progressively operates with the landslide emplacement. The distribution of fragment shape isotropy of the modeled deposit agrees well with that observed in the real system.

(d) When particle strength increases, the fragmentation degree first drops significantly and then increases following a
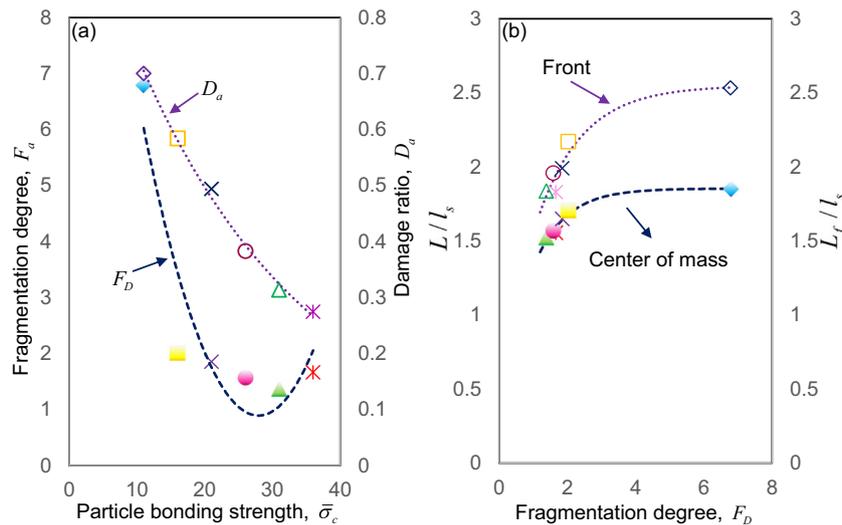
Fig. 17 a Variations of degree of fragmentation and damage ratio with the particle bonding strength. **b** The travel distance of the center of slope mass and the displacement of the front of the deposits with the degree of fragmentation

parabolic relationship; however, the damage ratio decreases exponentially. The increased travel length of the front and the center mass of the deposits is found to increase with the fragmentation degree. This indicates that the greater the degree of fragmentation, the greater the runout. When the material is stronger, the deposit is rough and the proportion of clast to matrix progressively increases.

References

Alfaro P, Delgado J, Garcia-Tortosa FJ et al (2012) The role of near-field interaction between seismic waves and slope on the triggering of a rockslide at Lorca (SE Spain). Nat Hazards Earth Syst Sci 12:3631–3643

Åstrom JA, Ouchterlony F, Linna RP, Timonen J (2004) Universal dynamic fragmentation in D dimensions. Phys Rev Lett 92(245506–1)

Bowman ET, Take WA, Rait KL, Hann C (2012) Physical models of rock avalanche spreading behaviour with dynamic fragmentation. Can Geotech J 49(4):460–476

Borykov T, Mège D, Mangeney A, Richard P, Gurgurewicz J, Lucas A (2019) Empirical investigation of friction weakening of terrestrial and Martian landslides using discrete element models. Landslides 16:1121–1140

Cagnoli B, Piersanti A (2015) Grain size and flow volume effects on granular flow mobility in numerical simulations: 3-D discrete element modeling of flows of angular rock fragments. J Geophys Res 120(4):2350–2366

Campbell CS (1990) Rapid granular flows. Annu Rev Fluid Mech 22(1):57–90

Crosta GB, Chen H, Lee CF (2004) Replay of the 1987 Val Pola Landslide, Italian Alps. Geomorphology 60:127–146

Crosta GB, Frattini P, Fusi N (2007) Fragmentation in the Val Pola rock avalanche. Italian Alps. J Geophys Res 112:F01006

Cui FP, Xu Q, Tan RJ, Yin YP (2011) Numerical simulation of collapsing and sliding response of slope triggered by seismic dynamic action. J TongJi Univ (Nat Sci) 39(3):446–450 (in Chinese)

Dammeier F, Moore JR, Haslinger F, Loew S (2011) Characterization of alpine rockslides using statistical analysis of seismic signals. J Geophys Res 116(F4):F04024

Dai FC, Xu C, Yao X, Xu L, Tu XB, Gong QM (2011) Spatial distribution of landslides triggered by the 2008 Ms 8.0 Wenchuan earthquake, China. J Asian Earth Sci 40(4):883–895

Dai Z, Huang Y, Cheng H, Xu Q (2014) 3D numerical modeling using smoothed particle hydrodynamics of flow-like landslide propagation triggered by the 2008 Wenchuan earthquake. Eng Geol 180:21–33

Davies TH (1982) Spreading of rock avalanche debris by mechanical fluidization. Rock Mech 15(1):9–24

Davies TR, McSaveney MJ, Hodgson KA (1999) A fragmentation-spreading model for long-runout rock avalanches. Can Geotech J 36(6):1096–1110

Davies TH, McSaveney MJ (2009) The role of dynamic rock fragmentation in reducing frictional resistance to large landslides. Eng Geol 109:67–79

Davies TRH, Reznichenko NV, McSaveney MJ (2020) Energy budget for a rock avalanche: fate of fracture-surface energy. Landslides 17:3–13

De Blasio FV, Crosta G (2014) Simple physical model for the fragmentation of rock avalanches. Acta Mech 225(1):243–252

De Blasio FV, Crosta GB (2015) Fragmentation and boosting of rock falls and rock avalanches. Geophys Res Lett 42(20):8463–8470

De Blasio FV, Elverhøi A (2008) A model for frictional melt production beneath large rock avalanches. J Geophys Res 113:F02014

Dufresne A, Geertsema M (2020) Rock slide–debris avalanches: flow transformation and hummock formation, examples from British Columbia. Landslides 17:15–32

Dunning SA (2006) The grain-size distribution of rock avalanche deposits in valley-confined settings. Ital J Eng Geol Environ 1:117–121

Eberhardt E, Stead D, Coggan J (2004) Numerical analysis of initiation and progressive failure in natural rock slopes the 1991 Randa rockslide. Int J Rock Mech Min Sci 41(1):69–87

Elmo D, Stead D, Eberhardt E, Vyazmensky A (2013) Applications of finite/discrete element modeling to rock engineering problems. Int J Geomech 13(5):565–580

Feng ZY, Lo CM, Lin QF (2017) The characteristics of the seismic signals induced by landslides using a coupling of discrete element and finite difference methods. Landslides 14(2):661–674

Fityus S, Giacomini A, Buzzi O (2013) The significance of geology for the morphology of potentially unstable rocks. Eng Geol 162:43–52

Gao G, Meguid MA (2018) On the role of sphericity of falling rock clusters- Insights from experimental and numerical investigations. Landslides 15(2):219–232

Gischig V, Eberhardt E, Moore JR, Hungr O (2015) On the seismic response of deep-seated rock slope instabilities-insights from numerical modelling. Eng Geol 193:1–18

Gu J, Zhao ZY (2009) Considerations of the discontinuous deformation analysis on wave propagation problems. Int J Numer Anal Methods Geomech 33(12):1449–1465

Haug ØT, Rosenau M, Leever K, Oncken O (2016) On the energy budgets of fragmenting rockfalls and rockslides: Insights from experiments. J Geophys Res Earth 121:1310–1327

Hou TX, Xu Q, Zhou JW (2015) Size distribution, morphology and fractal characteristics of brittle rock fragmentations by the impact loading effect. Acta Mech 226(11):3623–3637

Huang Y, Zhang W, Xu Q, Xie P, Hao L (2012) Run-out analysis of flow-like landslides triggered by the Ms 8.0 2008 Wenchuan earthquake using smoothed particle hydrodynamics. Landslides 9(2):275–283

Hungr O, Leroueil S, Picarelli L (2014) The Varnes classification of landslide types, an update. Landslides 11(2):167–194

Imre B, Laue J, Springman S (2010) Fractal fragmentation of rocks within sturzstroms: Insight derived from physical experiments within the ETH geotechnical drum centrifuge. Granul Matter 12(3):267–285

Itasca Consulting Group. (2014) Particle flow code in three dimensions (PFC^{2D} 5.0), Minneapolis

Kuhlemeyer RL, Lysmer J (1973) Finite element method accuracy for wave propagation problems. J Soil Mech Foundations Div ASCE 99:421–427

Legros F (2002) The mobility of long-runout landslides. Eng Geol 63(3-4):301–331

Levy S, Molinari JF, Vicari I, Davison A (2010) Dynamic fragmentation of a ring: predictable fragment mass distributions. Phys Rev E 82(6):066105

Langlois VJ, Quiquerez A, Allemand P (2015) Collapse of a two-dimensional brittle granular column: implications for understanding dynamic rock fragmentation in a landslide. J Geophys Res Earth Surf 120(1866–1880):JF003330

Li X, Wu Y, He S, Su L (2016) Application of the material point method to simulate the post-failure runout processes of the Wangjiayan landslide. Eng Geol 212:1–9

Lo CM, Lin ML, Tang CL, Hu JC (2011) A kinematic model of the Hsiaolin landslide calibrated to the morphology of the landslide deposit. Eng Geol 123:22–39

Locat P, Couture R, Leroueil S, Locat J, Jaboyedoff M (2006) Fragmentation energy in rock avalanches. Can Geotech J 43(8):830–851

Ma G, Zhou W, Regueiro RA, Wang Q, Chang XL (2017) Modeling the fragmentation of rock grains using computed tomography and combined FDEM. Powder Technol 308:388–397

Ma G, Zhou W, Zhang Y, Wang Q, Chang X (2018) Fractal behavior and shape characteristics of fragments produced by the impact of quasi-brittle spheres. Powder Technol 325:498–509

Martino S, Bozzano F, Caporossi P, D'Angiò D, Della Seta M, Esposito C, Fantini A, Fiorucci M, Giannini LM, Iannucci R, Marmoni GM, Mazzanti P, Missori C, Moretto S, Piacentini D, Rivellino S, Romeo RW, Sarandrea P, Schilirò L, Troiani F, Varone C (2019) Impact of landslides on transportation routes during the 2016–2017 Central Italy seismic sequence. Landslides 16:1221–1241

Meunier P, Hovius N, Haines AJ (2007) Regional patterns of earthquake-triggered landslides and their relation to ground motion. Geophys Res Lett 34:L20408

Hungr O, McDougall S (2009) Two numerical models for landslide dynamic analysis. Comput Geosci 35:978–992

Pedrazzini A, Jaboyedoff M, Loye A, Derron MH (2013) From deep seated slope deformation to rock avalanche: destabilization and transportation models of the Sierre landslide (Switzerland). Tectonophysics 605:149–168

Perinotto H, Schneider JL, Bachèlery P, Bourdonnec FXL, Famin V, Michon L (2015) The extreme mobility of debris avalanches: a new model of transport mechanism. J Geophys Res Solid Earth 120:8110–8119

Pollet N, Schneider JL (2004) Dynamic disintegration processes accompanying transport of the Holocene Flims sturzstrom (Swiss Alps). Earth Planet Sc Lett 221(1–4):433–448

Potyondy DO, Cundall PA (2004) A bonded-particle model for rock. Int J Rock Mech Min Sci 41(8):1329–1364

Ruiz-Carulla R, Corominas J, Mavrouli O (2015) A methodology to obtain the block size distribution of fragmental rockfall deposits. Landslides 12(4):815–825

Ruiz-Carulla R, Corominas J, Mavrouli O (2017) A fractal fragmentation model for rockfalls. Landslides 14:875–889

Sassa K, Wang G, Fukuoka H, Wang F, Ochiai T, Sugiyama M, Sekiguchi T (2004) Landslide risk evaluation and hazard zoning for rapid and long-travel landslides in urban development areas. Landslides 1(3):221–235

Scaringi G, Fan X, Xu Q, Liu C, Ouyang C, Domènech G, Yang F, Dai L (2018) Some considerations on the use of numerical methods to simulate past landslides and possible new failures: the case of the recent Xinmo landslide (Sichuan, China). Landslides 15:1359–1375

Shen WG, Zhao T, Crosta GB, Dai F (2017) Analysis of impact induced rock fragmentation using a discrete element approach. Int J Rock Mech Min Sci 98:33–38

Stead D, Eberhardt E, Coggan JS (2006) Developments in the characterization of complex rock slope deformation and failure using numerical modelling techniques. Eng Geol 83:217–235

Song YX, Huang D, Zeng B (2017) GPU-based parallel computation for discontinuous deformation analysis (DDA) method and its application to modelling earthquake-induced landslide. Comput Geotech 86:80–94

Taberlet N, Richard P, Jenkins JT, Delannay R (2007) Density inversion in rapid granular flows: the supported regime. Eur Phys J E: Soft Matter 22(1):17–24

Tang CL, Hu JC, Lin ML, Angelier J, Lu CY, Chan YC, Chu HT (2009) The Tsaoling landslide triggered by the Chi-Chi earthquake, Taiwan: insights from a discrete element simulation. Eng Geol 106(1):1–19

Thompson N, Bennett MR, Petford N (2009) Analyses on granular mass movement mechanics and deformation with distinct element numerical modeling: implications for large-scale rock and debris avalanches. Acta Geotech 4:233–247

Thornton C, Yin KK, Adams MJ (1996) Numerical simulation of the impact fracture and fragmentation of agglomerates. J Phys D Appl Phys 29(2):424–435

Turcotte DL (1986) Fractals and fragmentation. J Geophys Res Solid Earth 91(B2):1921–1926

Timár G, Blömer J, Kun F, Hermann HJ (2010) New universality class for fragmentation of plastic materials. Phys Rev Lett 104:095502

Wang C, Tannant DD, Lilly PA (2003) Numerical analysis of the stability of heavily jointed rock slopes using PFC2D. Int J Rock Mech Min Sci 40:415–424

Wang FW, Cheng QG, Highland L, Miyajima M, Wang H, Yan C (2009) Preliminary investigation of some large landslides triggered by the 2008 Wenchuan earthquake, Sichuan Province, China. Landslides 6:47–54

Wang YF, Cheng QG, Zhu Q (2015) Surface microscopic examination of quartz grains from rock avalanche basal facies. Can Geotech J 52(2):167–181

Wang YF, Cheng QG, Lin QW, Yang HF (2018) Insights into the kinematics and dynamics of the Luanshibao rock avalanche (Tibetan Plateau, China) based on its complex surface landforms. Geomorphology 317:170–183

Wang YF, Dong JJ, Cheng QG (2017) Velocity-dependent frictional weakening of large rock avalanche basal facies: implications for rock avalanche hypermobility? J Geophys Res Solid Earth 122:1648–1676

Wei J, Zhao Z, Xu C, Wen Q (2019) Numerical investigation of landslide kinetics for the recent Mabian landslide (Sichuan, China). Landslides 16:2287–2298

Wu J, Lin J, Chen C (2009a) Dynamic discrete analysis of an earthquake-induced largescale landslide. Int J Rock Mech Min 46:397–407

Wu JH, Chen CH (2011) Application of DDA to simulate characteristics of the Tsaoling landslide. Comput Geotech 38:741–750

Wu JP, Huang Y, Zhang TZ, Ming YH, Fang LH (2009b) Aftershock distribution of the MS 8.0 Wenchuan earthquake and 3-D P-wave velocity structure in and around source region. Chin J Geophys 52(1):102–111

Xu G, Li Z, Li P (2013) Fractal features of soil particle-size distribution and total soil nitrogen distribution in a typical water shed in the source area of the middle Dan River, China. Catena 101:17–23

Xu Q, Dong XJ (2009) Wangjiayan landslide, Beichuan in Xu Q, Pei XJ, Huang RQ (eds) Large-scale landslides induced by the Wenchuan earthquake. Science Press, Beijing, pp 174–187 (in Chinese)

Yerro A, Pinyol Núria M, Alonso EE (2016) Internal progressive failure in deep-seated landslides. Rock Mech Rock Eng 49(6):2317–2332

Yin Y, Wang F, Sun P (2009) Landslide hazards triggered by the 2008 Wenchuan earthquake, Sichuan, China. Landslides 6(2):139–152

Yin YP, Li B, Wang WP (2015) Dynamic analysis of the stabilized Wangjiayan landslide in the Wenchuan Ms 8.0 earthquake and aftershocks. Landslides 12(3):537–547

Yuan RM, Tang CL, Hu JC, Xu XW (2014) Mechanism of the Donghekou landslide triggered by the 2008 Wenchuan earthquake revealed by discrete element modeling. Nat Hazards Earth Syst Sci 14:1195–1205

Yuan RM, Tang CL, Deng Q (2015) Effect of the acceleration component normal to the sliding surface on earthquake-induced landslide triggering. Landslides 12:335–344

Zhang M, McSaveney M (2017) Rock avalanche deposits store quantitative evidence on internal shear during runout. Geophys Res Lett 44:8814–8821

Zhang M, Yin YP, Wu SR, Zhang YS, Han JL (2011) Dynamics of the Niumiangou creek rock avalanche triggered by 2008 May 12 Wenchuan Ms8.0 earthquake, Sichuan, China. Landslides 8(3):363–371

Zhang M, Wu L, Zhang J, Li L (2019) The 2009 Jiweishan rock avalanche, Wulong, China: deposit characteristics and implications for its fragmentation. Landslides 16:893–906

Zhang M, Yin YP, McSaveney M (2016) Dynamics of the 2008 earthquake-triggered Wenjiagou Creek rock avalanche, Qingping, Sichuan, China. Eng Geol 200:75–87

Zhang YH, Fu XD, Sheng Q (2014) Modification of the discontinuous deformation analysis method and its application to seismic response analysis of large underground caverns. Tunn Undergr Space Technol 40:241–250

Zhang Y, Wang J, Xu Q, Chen G, Zhao J, Zheng L, Han Z, Yu P (2015) DDA validation of the mobility of earthquake-induced landslides. Eng Geol 194:38–51

Zhao T, Crosta GB (2018) On the dynamic fragmentation and lubrication of coseismic landslides. J Geophys Res Solid Earth 123:9914–9932

Zhao T, Crosta GB, Dattola G, Utili S (2018) Dynamic fragmentation of jointed rock blocks during rockslide-avalanches: insights from discrete element analyses. J Geophys Res Solid Earth 123:1–20

Zhou W, Lai Z, Ma G, Yang L, Chen Y (2016) Effect of base roughness on size segregation in dry granular flows. Granul Matter 18(4):83

Zhou JW, Huang KX, Shi C, Hao MH, Guo CX (2015) Discrete element modeling of the mass movement and loose material supplying the gully process of a debris avalanche in the Bayi gully, Southwest China. J Asian Earth Sci 99:95–111

G. Gao · **M. A. Meguid** (✉) · **L. E. Chouinard**
Civil Engineering and Applied Mechanics,
McGill University,
817 Sherbrooke St. W., Montreal, Quebec, H3A 0C3, Canada
Email: mohamed.meguid@mcgill.ca

G. Gao
e-mail: ge.gao2@mail.mcgill.ca

L. E. Chouinard
e-mail: luc.chouinard@mcgill.ca

W. Zhan
Glenn Department of Civil Engineering,
Clemson University,
Clemson, SC 29634, USA
e-mail: wzhan@clemson.edu